CHALMERS
UNIVERSITY OF TECHNOLOGY

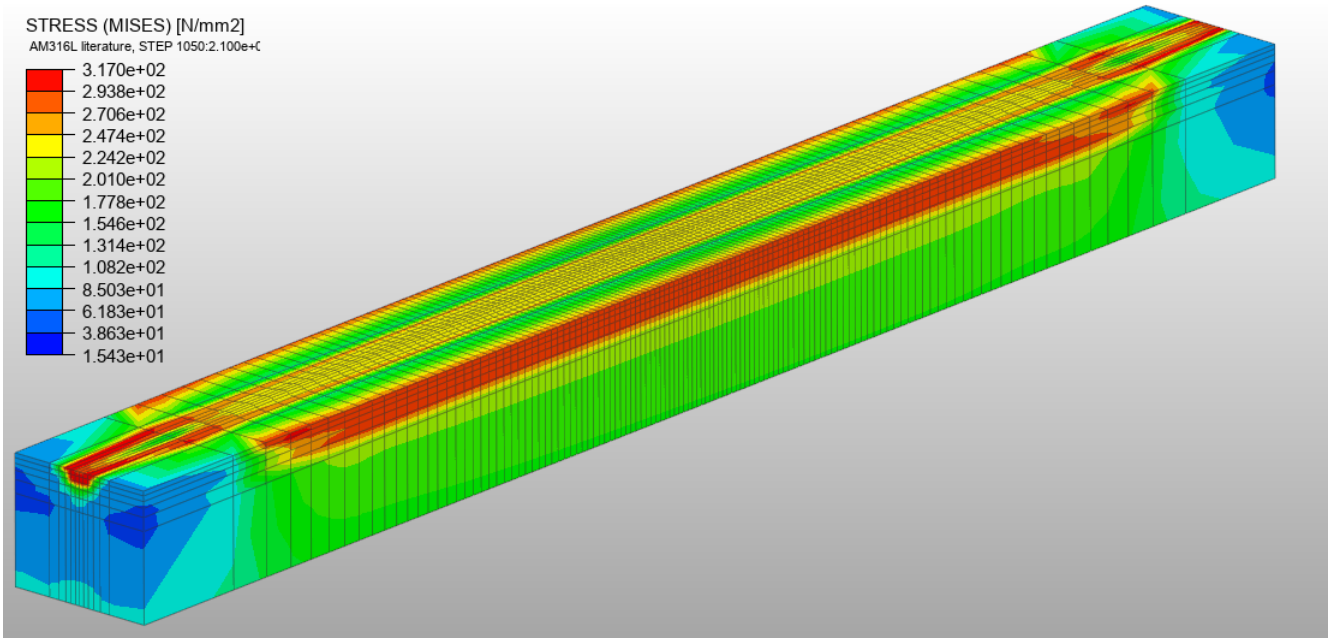

Residual stress modelling for PBF-LB

A study of AdditiveLab as a meso-scale simulation tool in laser powder bed fusion

Master's thesis in Master Program Structural Engineering and Building Technology

Haukur Friðriksson

Department of Industrial and Materials Science - IMSX30
CHALMERS UNIVERSITY OF TECHNOLOGY
Gothenburg, Sweden 2024
www.chalmers.se

Master's thesis IMSX30-xx-xx

Residual stress modeling of PBF-LB

A study of Additive Lab as a meso-scale simulation tool in laser powder bed fusion

Master's thesis in Master Program Structural engineering and building technology

Haukur Friðriksson

CHALMERS
UNIVERSITY OF TECHNOLOGY

Division of Material and Computational Mechanics
Department of Industrial and Materials Science
Chalmers University of Technology
Gothenburg, Sweden 2024

Sensitivity of L-PBf process simulations in Additive Lab
Master's thesis in Master Program Structural engineering and building technology

Haukur Friðriksson

Main Supervisor: Professor Ragnar Larsson, Department of Material and Computational Mechanics
co-Supervisor: David Ohlsson, RISE Research Institutes of Sweden
Examiner: Professor Ragnar Larsson, Department of Material and Computational Mechanics

Division of Material and Computational Mechanics
Department of Industrial and Materials Science
Chalmers University of Technology
SE-412 96 Gothenburg
Telephone +46 31 772 1000

Department of Architecture and Civil Engineering
Gothenburg, Sweden 2024

Residual stress modeling of PBF-LB
A study of AdditiveLab as a meso-scale simulation tool in laser powder bed fusion
Haukur Friðriksson
Division of Material and Computational Mechanics
Chalmers University of Technology

Abstract

This thesis investigates the modeling of residual stress in laser powder bed fusion (PBF-LB) processes using AdditiveLab as a meso-scale simulation tool. The study aims to evaluate AdditiveLab as a process simulations tool for PBF-LB by replicating experimentally verified simulations, specifically focusing on 316L stainless steel. A literature review of simulation techniques was conducted, followed by transient thermal and thermo-mechanical simulations, and validation of AdditiveLab's simulations against experimentally verified models from the literature. The simulations analyzed the thermal distribution, the dimensions of the melt pool, and the development of residual stress.
The findings indicate that, while the moving heat source can be modeled using AdditiveLab, limitations of the possible material modeling negatively impact the accuracy of the temperature distribution in meso-scale simulations. The primary limitation being the phase change model, in which the density of the metal powder can only be modeled as being equal to the solid metal density. Although all mesoscale modeling involves simplifications of complex physical phenomena, the assumption of powder properties leads to an overestimation of powder thermal inertia, leading to an overestimation of the melt-pool temperature and an underestimation of the melt-pool depth and width. This thesis discusses these limitations and their impact on predicting thermal behavior and stress development.

Keywords: Laser Powder Bed Fusion, Additive Manufacturing, Meso-scale Simulation, AdditiveLab, Boundary Conditions, Heat Source Models, 316L Stainless Steel, Transient Thermal Simulation, Thermomechanical Simulation.

Acknowledgements

I would like to express my gratitude to my examiner Ragnar Larsson and supervisor David Ohlsson.

Haukur Friðriksson, Gothenburg, September 2024

Contents

List of Figures

List of Tables

1
Introduction

1.1 Background

Powder Bed Fusion-Laser Beam (PBF-LB) is a metal additive manufacturing (AM) method, it works by spreading a thin layer of metal powder and using a laser to selectively melt parts of it to make a cross section of a fused metal, then adding a new layer of powder on top and repeating the process to build a 3D object.

According to a research report from Swerim et al, the current state of the AM-industry does not meet the markets high expectations. The report identifies repeatability and part quality as typical challenges for the industry. For a repeatability challenge, there can be differences between builds with different machines, individual builds on the same machine, different batches of powder or within a build in different parts [1]. Chowdhury et al found that a main obstacle to the AM industry is the lack of a complete understanding of the connection between the process parameters and, the final part and material properties [2]. PBF-LB is a complex process with a high number of process parameters that need to be combined correctly to get a fully dense part. The major process parameters are laser power, scan speed, hatch spacing and layer thickness, they are combined to calculate laser energy density. Combinations of them are known as processing windows, they differ for each material [2]. Processing windows are generally found with trial and error experimentation on built parts. Experimentation on built parts gives information about material properties and defects although they do not show the mechanisms of how they form. Process monitoring is time consuming and costly to operate, and focuses on a single subject. [3] Numerical models are flexible and cheap in comparison to experiments. Physics can be implemented based on need for the studied phenomena [3].

The multi-physics and multi-scale nature of PBF-LB makes it challenging to simulate. Some phenomena happen on the order of microseconds while a complete build might take days. Simulating all relevant physical phenomena on the scale of whole parts is impossible on modern computers, so simulations are generally split into classes based on length scale and the physics included. Meso-scale focuses on small-scale phenomena of a limited section of a build, such as melt-pool behaviour or material micro structure. Part-scale focuses on modelling the entire build process of a part to predict macroscopic phenomena such as deformation, cracking or overheating. This is achieved by simplifying the simulations to lower computational costs [3].

Bayat et al found that convective transient thermal models are not very accurate

in predicting temperature distribution as they omit convective heat transfer in the melt-pool. Compared to multi-physics models, that are very accurate in predicting the melt-pool properties. However, they are much more complex and computationally costly [3].
One hurdle to the predictive capabilities of process simulation are the large number of environmental parameters. Conditions can vary a lot based on position in the build chamber or fraction of build chamber scanned in each layer. Variations in factors such as the position within the powder bed, the temperature distribution of the surrounding powder, and the velocity and direction of gas flow within the chamber can affect the melt pool properties and stress of the fused parts. A better understanding the sensitivity of the melt pool to different boundary conditions to make more predictive and accurate models.

1.2 Purpose

This thesis intends to provide an overview of the state of the art in meso-scale transient thermal and thermo- mechanical modelling of PBF-LB with a literature study. Study how the theory is implemented in AdditiveLab. To assess the sensitivity of the simulations to variations in boundary conditions using AdditiveLab. And replicate experimentally validated transient thermal and thermo-mechanical scanning path simulations in Additive Lab to evaluate the methods and results from AdditiveLab.

1.3 Scope

The literature study aims to cover the state of the art in transient thermal and thermo-mechanical meso-scale process as is relevant for the simulations using AdditiveLab, a novel software developed for additive manufacturing processes simulation [4]. The focus of the study are melt-pool temperature and dimensions, the temperature and stress history of single nodes. The variables in the sensitivity study are the top layer thermal boundary conditions. Using a material model for 316L steel in single trajectory scanning path simulations. The temperature distribution is predicted with a transient thermal simulation and compared against the results from Foroozmehr et al. [5]. The development of residual stresses is simulated with a thermomechanical simulation, and is compared against Hussein et al. [6].

1.4 Method

Common and successful simulation methods and parameters are identified from a literature study and experimentally validated simulations are replicated. Different values for the thermal boundary conditions are used in the simulations to test the sensitivity melt-pool to them, the results are compared to Foroozmehrs results. A thermo-mechanical simulation was performed using the same parameters as those in the study by Hussein et al. [6] This simulation focused on analyzing the development of residual stresses during the PBF-LB process.

2

Theory

In this chapter, the relevant theory behind the simulations in AdditiveLab is covered, as well as some simplifications of the physics involved in the process for simulations.

As mentioned above, PBF-LB is a highly non linear process, with steep temperature and stress gradients in both time and space dimensions. Rapid heating of metals causes them to expand, and lowers the stiffness and yield strength. As the metal powder reaches the melting temperature, an abrupt change in material properties with the phase-change.

The molted powder forms a melt-pool with a thermal gradient. This drives a convective flow known as Bénard–Marangoni convection. The hotter regions of the melt-pool have lower surface tension than the colder regions, driving flow of hotter material towards the colder regions, increasing the local temperature there. This effect causes an increased heat transfer towards the deeper sections of the melt-pool compared to pure conduction [7]. The surface of the melt-pool exposed to the concentrated laser reaches extreme temperatures, causing substantial vaporisation of metal [8]. Vaporisation has high latent heat, and thus removes heat from the system, as well as removing material from the melt pool and subjecting its surface to increased vapor pressure. This added pressure can form a cavity in the melt-pool known as a key hole, speed up the flow caused by the Marangoni effect and affect the flow of protective gas around the melt pool [9]. This can lead to defect producing phenomena such as spattering, where the vapor pressure or turbulence in the Marangoni flow can eject particles to other sections of the build chamber [10], powder denudation, where powder clears from the laser beam, and key hole porosity where the key-hole cavity collapses in a way that leaves a pore in the fused metal. Depending on the process parameters, two main modes of heat transfer are dominant in PBF-LB, in lower energy density processes conduction is the main mode of heat transfer, and in higher energy density processes (key-hole mode melting), convection is the main mode of heat transfer [11]. In this thesis, only the lower energy processes are considered where conduction is the main mode of heat transfer. Including Bénard–Marangoni convection and effects of vaporization are vital to implement in order to fully model a PBF-LB process, however they are secondary effects of the thermal distribution and including them requires fluid dynamics simulations, that are both complex and computationally heavy. A simplification is made such that the material is modelled as a solid, and powder is assumed to be a continuum with a void ratio instead of being composed of solid particles and gas.

2.1 Thermal models

Pure thermal models aim to solve for the transient temperature field during the build process by solving the partial differential equation of heat conduction derived from energy balance when displacement is set to 0. The aim of transient thermal simulations is generally to predict melt-pool dimensions and temperature. The models ignore mechanical and fluid dynamics effects so the simulation parameters must be calibrated to fit experimental results. For this reason the intended use is mostly for predicting process sensitivity for optimizing parameters [3].

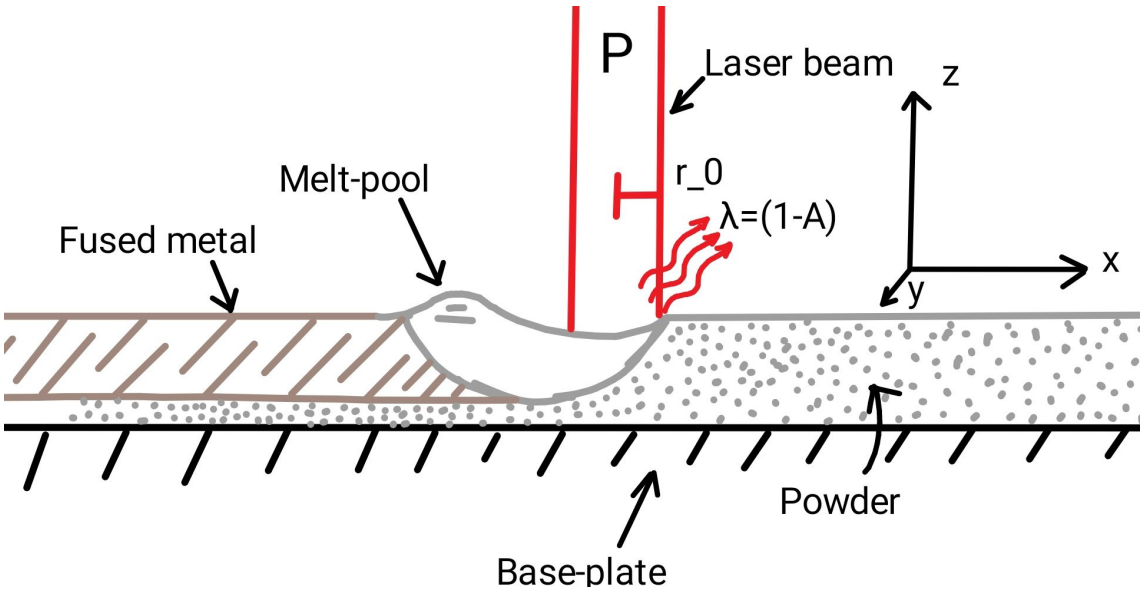

Figure 2.1: Schematic figure of the PBF-LB process on a thick powder layer that does not fuse with the base plate. P is the laser power in watts $[W]$, r_0 is the radius of the laser beam. λ is the reflectivity of the powder and A is the absorptivity of the powder.

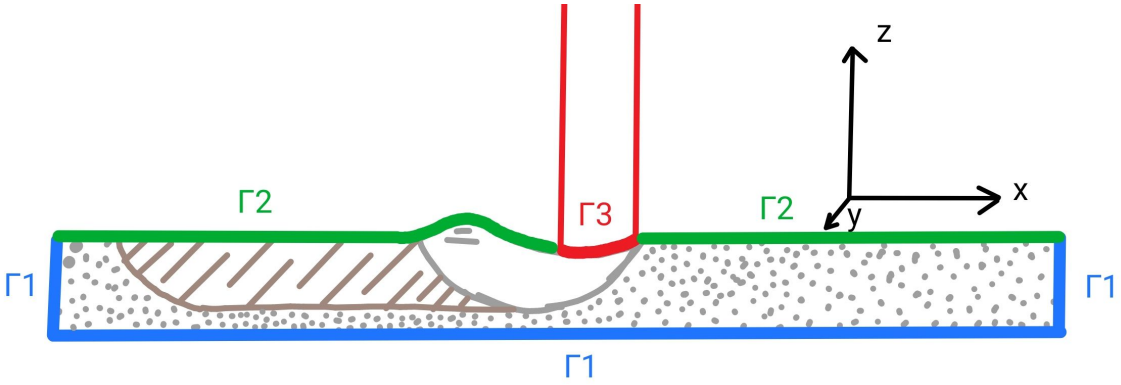

Figure 2.2: The different boundary conditions on each region of the domain. Γ1 is only convective. Γ2 is convective and radiative. Γ3 is convective, radiative and can have a known heat flux when the laser beam is modelled as a surface heat source.

Energy balance:

$$\rho c_p \frac{\partial T}{\partial t} = \nabla \cdot (k \nabla T) + Q \tag{2.1}$$

Where ρ is the density of the materials (bulk metal, liquid metal and powder) $[kg/m^3]$, density is a factor in determining the thermal inertia of the material. In transient thermal modelling, density values must be given for a temperature range the material is not allowed to expand. c_p is the specific heat (or heat capacity) of the materials $[J/kgK]$, it is the first derivative of enthalpy, while the ethalpy is a measure of the energy of the matter for a given temperature, the specific heat is a measure of the energy difference per unit mass in a material for 1°C cooling or heating. Along with density they represent the thermal inertia. T is temperature of the material $[\deg C]$, it is the primay variable being solved for, and is the load that drives any phenomena in higher complexity simulations. t is time $[s]$. ∇ is the divergence operator $(\frac{\partial}{\partial x}, \frac{\partial}{\partial y}, \frac{\partial}{\partial z})$), it separates the flow components into the three axes. k is the conductivity $[W/mK]$, a measure of how quickly heat spreads throughout the material. Q is heat supply from the laser $[W/m^3]$ and acts as the only load on the system. Density, specific heat, and conductivity are temperature dependent, with density lowering with increased temperature, though specific heat and conductivity typically increase with increasing temperature.
The boundary regions are marked in figure 2.2, The regions are $\Gamma 1 : q_{conv}$, $\Gamma 2 : q_{conv} + q_{rad}$ and $\Gamma 3 : q_{conv} + q_{rad} + q_{laser}$ if the laser is modelled as a surface heat source, or $\Gamma 3 = \Gamma 2 : q_{conv} + q_{rad}$ if the laser is modelled as a volumetric heat source. Also represented in equation (2.2)

$$-k\frac{\partial T}{\partial \mathbf{n}} = \begin{cases} q_{conv} & (x,y,z) \in \Gamma 1 \\ q_{conv} + q_{rad} & (x,y,z) \in \Gamma 2 \\ q_{conv} + q_{rad} + q_{laser} & (x,y,z) \in \Gamma 3 \end{cases} \tag{2.2}$$

Where:
k is the thermal conductivity of the material $[W/mk]$
T is temperature of the surface $[\deg C]$
$\mathbf{n}$ is the normal vector to the surface of the powder
q_{conv} is convective heat flux $[W/m^2]$ explaned in eq. (2.3)
q_{rad} is heat radiative flux $[W/m^2]$ explaned in eq. (2.4)
q_s represents the laser beam modelled as a surface heat flux $[W/m^2]$ explaned in eq. (2.5)
Convective Boundary:

$$q_{conv} = h(T - T_{amb}) \tag{2.3}$$

Where:
q_{conv} is convective heat flux $[W/m^2]$
h is the convection coefficient $[W/m^2K]$
T_{amb} is the temperature of the ambient air in the build chamber
Radiation Boundary:

$$q_{rad} = \epsilon\sigma(T^4 - T_{amb}^4) \tag{2.4}$$

Where:
q_{rad} is heat radiative flux $[W/m^2]$

T is the temperature of the material in kelvin, and T_{amb} is the ambient air temperature in the build chamber in Kelvin.

ϵ is emissivity of the surface material $[-]$

σ Stefan Boltzmann constant $= 5.67 \cdot 10^{-}11 W/mm^2K^4$

Heat flux:

$$q_{laser} = q_s \tag{2.5}$$

Where: q_s represents the laser beam modelled as a surface heat flux as in equation (2.7).

For this thesis, a simplification is made so that the ambient temperature is fixed, in a real PBF-LB process there will be great fluctuation of the temperature in the build chamber.

Initial temperature:

$$T(x, y, z, t = 0) = T_0(x, y, z) \tag{2.6}$$

The heat supply represents the laser, and for low laser powers and scan speeds, it is most common to model the heat source as a Gaussian distribution surface heat flux as in (2.7) or volumetric heat flux, with a Gaussian distribution in the x-y plane and evenly distributed in the z depth direction. Usually similar to equation (2.8). Both models are only applicable to lower energy density processes, as both the shape of the melt-pool and the primary mode of heat conduction change with increased energy density. The surface Gaussian distribution described in (2.7) tends to underestimate depth of the melt pool more than the volumetric source in (2.8) as only heat conduction from the surface is considered.

$$q_s(r) = \frac{2AP}{\pi r_0^2} e^{-2(\frac{r}{r_0})^2} \tag{2.7}$$

$$Q(r, z) = \frac{2AP}{\pi r_0^2 d} e^{-2(\frac{r}{r_0})^2} \tag{2.8}$$

where Q is the beam intensity at a point r from the beam center, here the distribution over z is uniform $[W/m^3]$. q_s is the beam intensity at a point r from the beam center $[W/m^2]$. A is the energy absorption coefficient of the powder $(1 - \lambda)$ where λ is the reflectivity of the powder $[-]$, a simplification is made that reflectivity is constant for any temperature. P is the laser power $[W]$. r is the distance from the center of the spot $[m]$. r_0 is the spot radius $[m]$. d is the optical penetration depth (OPD) $[m]$, it is defined as the depth at which the beam intensity is a fraction $1/e$ of the intensity at the surface due to scattering in the powder as is shown in figure 2.3. A simplification made in this model is that the intensity is evenly distributed down to the OPD instead of decreasing exponentially. Thus underestimating the intensity at the surface and overestimating it at the OPD.

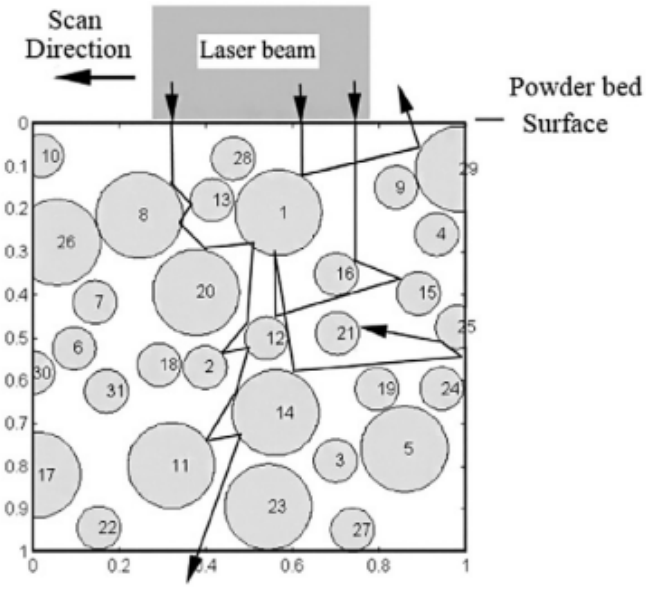

Figure 2.3: Figure is from Foroozmehr 2016, shows the light interacting with the powder bed. the light scatters in the powder.

Figure 2.4 shows the distribution of the laser beam energy following the distribution in equation (2.7). The heat supply described in equation (2.7) follows the same distribution integrated over the depth.

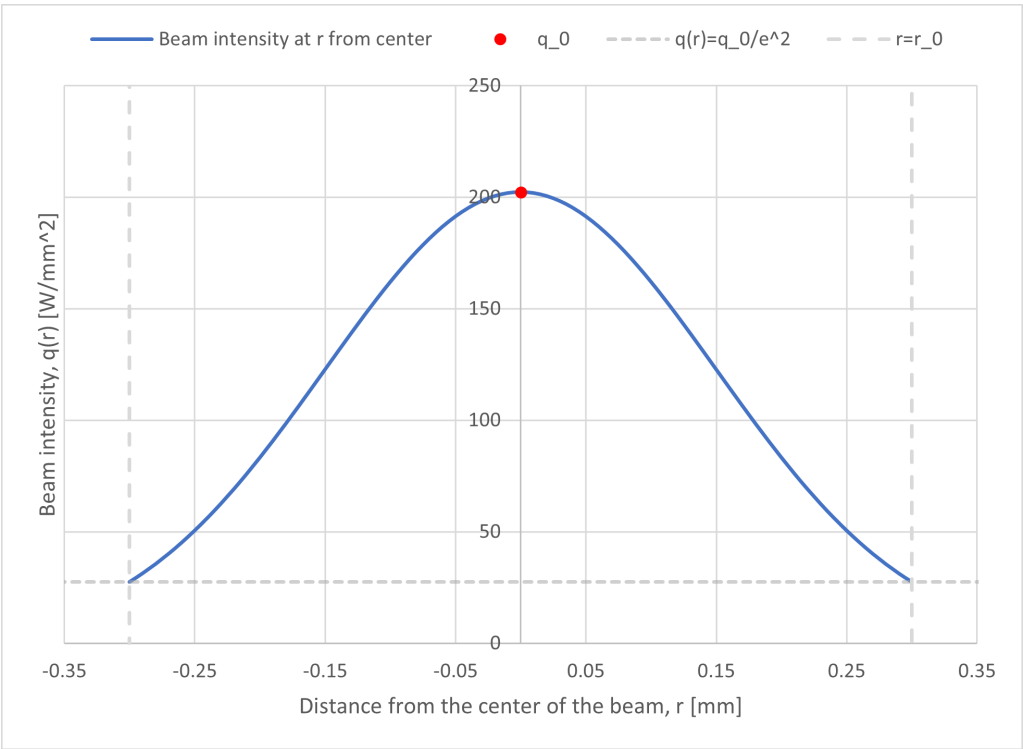

Figure 2.4: The beam intensity distribution of a surface Gaussian heat source with P=110W, A=0.52 and r_0=0.3mm.

Foroozmher et al. [5] developed a numerical transient thermal FE model for process simulations with 316L steel. Using a volumetric heat load where the heat intensity was distributed uniformly in the plane and following a Gaussian distribution in the depth, reaching $1/e$ fraction of the surface beam intensity at the Optical Penetration Depth (OPD). The OPD was based on an extrapolation from earlier experiments of similar powders [5] [12]. Furthermore modeling the spot as a square with the same area as a circle with the laser diameter. The absorption coefficient was 0.52 based on recommendation from previous studies with carbon lasers and similar powder [13]. The boundary condition at the surface of the powder bed ($\Gamma 1$ and $\Gamma 2$ in figure 2.2) was assumed to be only convection, omitting emissivity. Comparison with experimental results showed good results in predicting layer thickness, especially in subsequent passes of the laser. they found that the melt pool width and depth varies over time, growing until it reaches a steady state, and that the melt pool reaches higher average temperatures when scanning next to earlier tracks.
Li and Go [14] investigated the effects of scanning speed and laser power on the thermal behaviour of pure titanium. They used a moving surface Gaussian heat source model, where the heat flux at the edge of the spot was $1/e^2$ of the peak value in the center. This distribution is the most common Gaussian distribution used in heat source modeling shown in equation (2.7). They found that doubling the laser power had a greater effect on the temperature and liquid lifetime of the melt pool than decreasing the scanning speed by half.
Criales et al. [15] investigated the sensitivity of a PBF-LB process simulation with inconel 625 to variations in laser power, scanning speed and powder properties (Bulk density (ρ_{pow}), conductivity k, latent heat of fusion, specific heat C_p and reflectivity λ by $\pm 10\%$. Using a moving surface Gaussian heat source with the same distribution as in equation (2.7). They found that the largest effect on peak temperature was the material reflectivity and laser power, which both affect the beam intensity directly. Reflectivity, laser power and scanning speed had the most influence on the melt pool geometry. Variations in laser spot diameter and latent heat of fusion had very little effect on the melt pool length and geometry, with spot diameter still significantly affecting the peak temperature. The bulk density of the power had a significant effect on all the melt pool parameters.
Fu and Gou (2014) [16], made a thermal PBF-LB model in Abaqus using a moving Gaussian heat source and Ti-6Al-4V powder. They present a shape factor for an alternative distribution of the Gaussian laser. The shape factor affects the width of the distribution, and the fraction of the peak intensity at the spot radius.

$$q(r) = \frac{SfactAP}{\pi r_0^2} e^{-Sfact(\frac{r}{r_0})^2} \tag{2.9}$$

Where Sfact is a dimensionless shape factor that affects the shape of the Gaussian Distribution. A higher Sfact concentrated more of the laser energy to the center of the laser spot. Note that equation (2.9) is the same as (2.7) if Sfact is taken as 2.
Recently a ring shaped heat source has been utilized more to prevent the excessively high energy concentration in the center of the spot with Gaussian distribution. High power lasers cause spattering, keyhole formations and powder denudation [17]. According to Rasch et al. [18], distribution poses a bigger problem than the intensity.

A ring shape laser addresses those problems with a more even temperature distribution over the scanned area, allowing for a larger process window.
Grünewald et al. [19] studied the effects of different ring shape distributions and compared to Gaussian distribution using a 316L substrate without powder. They found that with a ring shaped laser, much higher power and scanning speed can be achieved without compromising the stability of the process. Allowing for increased productivity. Ring lasers have a significantly larger spot size than Gaussian lasers and thus lead to a lower resolution.
In a study by Mohammadpour et al. [20] using an adjustable ring laser that could switch between a ring shape with high intensity on the rim to a higher intensity in the center or a flat top distribution. They found through experiments that the ring shape reduced penetration depth and drastically reduced splattering.

2.1.1 Phase change

A common model for phase change is one that is described in Foroozmehr et al. [5]. Powder, solid metal and liquid metal are all treated as solids. Powder is then modelled to have conductivity, and density and specific heat that are a fraction of the solid metal properties, as is described in equations (2.10), (2.11) and (2.12). As the powder reaches melting temperature, the material properties of powder switch to those of solid metal.

$$k_{powder} = \begin{cases} 0.01k_{solid} & T \leq T_{melt} \\ k_{solid} & T_{melt} \leq T \end{cases} \tag{2.10}$$

where:
k_{powder} is the conductivity of powder $[W/mK]$
k_{solid} is the conductivity of the solid metal $[W/mK]$
T is the temperature of the powder $[\deg C]$
T_{melt} is the melting temperature $[\deg C]$

$$\rho_{powder} = \phi\rho_{gas} + (1-\phi)\rho_{solid} \tag{2.11}$$

$$\rho_{powder}C_{p,powder} = \phi\rho_{gas}C_{p,gas} + (1-\phi)\rho_{solid}C_{p,solid} \tag{2.12}$$

where:
ρ_{powder} is the density of powder. $[kg/m^3]$
ρ_{gas} is the density of gas. $[kg/m^3]$
ρ_{solid} is the density of solid material. $[kg/m^3]$
ϕ is the void ratio of the powder. $[-]$
$C_{p,powder}$ is the heat capacity of powder. $[J/kgK]$
$C_{p,gas}$ is the heat capacity of the gas. $[J/kgK]$
$C_{p,solid}$ is the heat capacity of the solid. $[J/kgK]$
$\rho_{powder}C_{p,powder}$ is the volumetric heat capacity of powder. $[J/m^3K]$
During phase change, a significant amount of heat is absorbed as the material transitions from solid to liquid state, this heat is then released as the material transitions from liquid to solid. In materials with constant melting temperature, this latent

heat is absorbed or released at a constant temperature. Using a method called apparent heat capacity, this effect from the latent heat is captured as an increase in the specific heat at the temperature where phase change occurs instead of modelling the latent heat of fusion explicitly [21].

2.2 Thermomechanical models

A weakly coupled thermomechanical simulation works by first solving a transient thermal problem as was described in chapter 2.0.1, and using the temperature field as a load on a mechanical simulation [22]. Static equilibrium [3]:

$$\frac{\partial \sigma_{ij}}{\partial x_j} = o \tag{2.13}$$

$$\sigma_{ij} = \frac{E}{1-\nu}\left[\frac{1}{2}(\delta_{ik}\delta_{jl} + \delta_{il}\delta_{jk}) + \frac{\nu}{1-2\nu}\delta_{ij}\delta_{kl}\right]\epsilon^{el}_{kl} \tag{2.14}$$

strain:

$$\epsilon^{total}_{ij} = \epsilon^{el}_{ij} + \epsilon^{pl}_{ij} + \epsilon^{th}_{ij} \tag{2.15}$$

thermal expansion:

$$\epsilon^{th} = \alpha \Delta T \tag{2.16}$$

strain-displacement:

$$\epsilon_{ij} = \frac{1}{2}\left[\frac{\partial u_i}{\partial x_j} + \frac{\partial u_j}{\partial x_i}\right] \tag{2.17}$$

where: δ_{ij} is Kronecker's delta. ϵ^{el} is elastic strain, an instantaneous response following Hooke's law: $\epsilon^{el} = \mathbf{C}^{-1} : \sigma$, where $\mathbf{C}$ is the 4th order elasticity tensor that is $C_{ijkl} = \lambda\delta_{ij}\delta_{kl} + \mu(\delta_{ik}\delta_{jl} + \delta_{il}\delta_{jk})$ with $\lambda = E\nu/((1+\nu)(1-2\nu)$ and $\lambda = E/2(1+\nu)$ for isotropic materials.
ϵ^{pl} is plastic strain. When the Von Mises stress described in (2.18) exceeds the yield strength of the material the material deforms plastically, this yiled criterion is expressed as $f(\sigma) = \sigma_v - \sigma_y \leq 0$ where σ_y is the material yield strength. If the yield criterion is negative, the material is in an elastic region. The flow rule $\Delta\epsilon^p = \Delta\lambda_p \frac{\delta f}{\delta \sigma}$, here λ_p is a plastic multiplier that ensures the consistency of the yield criteria, and $\frac{\delta f}{\delta \sigma}$ is the plastic potential.
ϵ^{th} is thermal strain. Von Mieses stress:

$$\sigma_v = \frac{1}{\sqrt{2}}\sqrt{(\sigma_{11}-\sigma_{22})^2 + (\sigma_{22}-\sigma_{33})^2 + (\sigma_{33}-\sigma_{11})^2 + 6(\sigma^2_{12} + \sigma^2_{23} + \sigma^2_{13})} \tag{2.18}$$

Pure thermal models tend to overestimate the temperature of the melt pool [23] as they do not simulate the convective flow in the melt pool. Hussein et al. [6] developed a 3D finite element model to simulate temperature and stress fields in single layers built without support during PBF-LB process in ANSYS. Using a step wise moving Gaussian heat source to perform transient thermal analysis and use the temperature result as a load in a thermomechanical simulation. Hussein et al. used an elastic FEA simulation and an isotropic material model to predict the stress. The simulations were compared to experimental results and showed good predictive

capabilities for the temperature and stress fields, especially at the higher scanning speeds ($200mm/s$ and $300mm/s$), while underestimating the melt pool depth at the lower speed ($100mm/s$). This is likely due to the limitations of thermo-mechanical models, since they do not simulate convective heat trasnfer in the melt-pool: the model accuracy is very sensitive to changes to the process parameters they are calibrated for.

3
Methods

In this chapter the models created for this thesis and simulated are described with respect to geometrical data, discretization, material data and boundary conditions. Two modelleing approaches have been investigated. The first one is a transient thermmal simulation based on a paper by Foroozmehr et al. [5] and the second is a thermomechanical simulation based on a paper by Hussein et al. [6]. The simulation campaign has two main goals: The first is to assess the validity of thermal results from AdditiveLab against comparable simulations and experiments. The second is to simulate the development of residual stresses in the fused metal.

3.1 Model validation references

Foroosmehr et al. [5] ran a multi-trajectory transient-thermal scanning path simulation with 316L stainless steel with the setup shown in figure 3.1. The simulations were compared to a physical print of a single layer using the same process paramaters. The layer thickness from the FE simulations were on average 0.234mm compared to the experimental build of 0.230mm. This corresponds to an error rate of 1.6% and is considered as proof of the validity of the simulations. The design of the simulations in this thesis is based on the framework established by Foroozmehr's and Hussein's simulations adapted for Additice Lab Reasearch Version 5. The process parameters and some of the boundary conditions used are shown in table 3.2.

Process parameter	**Start of track**
Laser power, P $[W]$	110
Layer thickness, $[mm]$	1
Laser Spot size, r_0 $[mm]$	0.3
Scanning speed, V $[mm/s]$	100
Track length $[mm]$	4.5
Absorption rate of powder from eq. (2.8), A $[-]$	0.52
optical penetration depth, (OPD) $[mm]$	0.12
Top layer convection coefficient, q_{conv} $[mW/mm^2k]$	0.01
Top layer emissivity coefficient, q_{rad} $[-]$	0.0

Table 3.1: Process parameters and boundary conditions in Foroozmehr et al. [5] and the transient thermal simulation for comparisons in this thesis.

The final simulation of this thesis is a thermo-mechanical simulation, the process

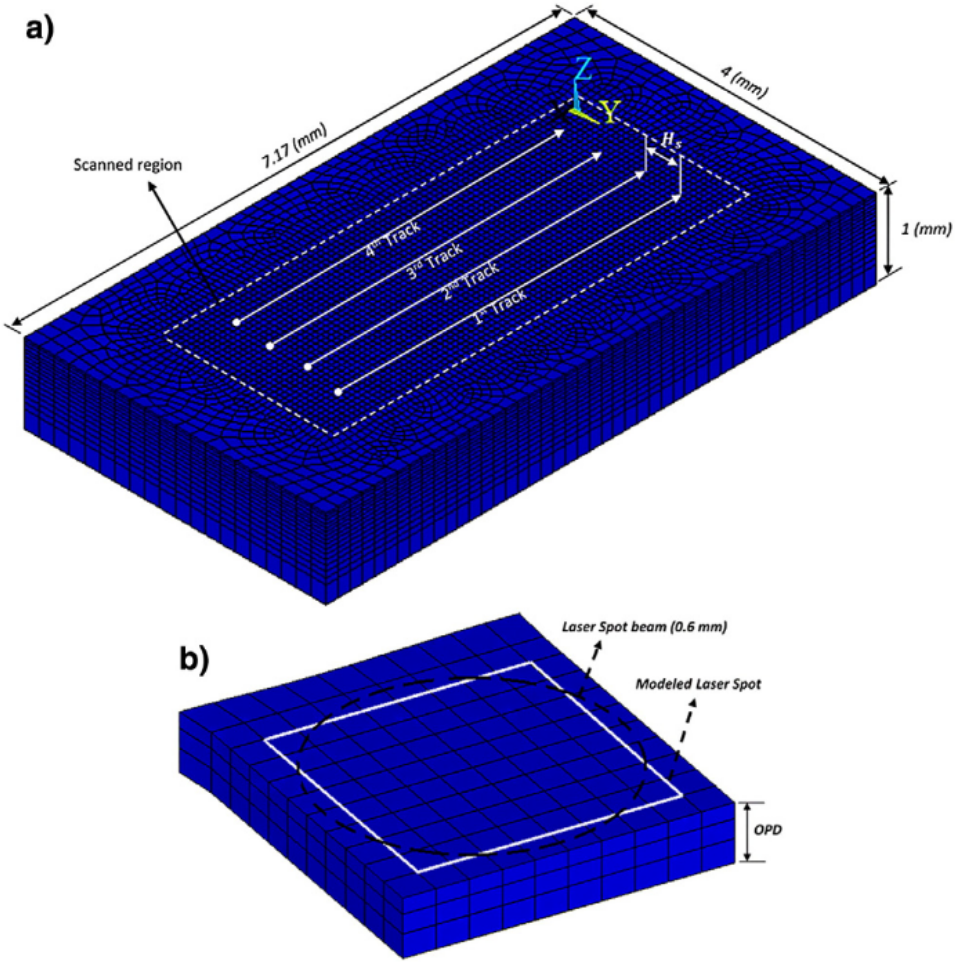

Figure 3.1: from Foroozmehr et al. [5], The simulation setup for the multi-trajectory scanning path simulation

parameters were selected to replicate the simulations of Hussein et al. [6]. Hussein developed a weakly coupled thermo-mechanical model in ANSYS by solving a transient thermal analysis step to obtain the temperature distribution and using that as a load for a mechanical simulation step. No external loads are applied to the mechanical system, so only the thermal expansion of the material in the constrained domain cause stresses.

Hussein ran a multi-trajectory thermo-mechanical simulation using an elastic material model to study the development of stress from the cyclic heating from scanning the adjacent trajectories. In this thesis, a simple plasticity model is added to the simulation using the yield strength data presented in Hussein et al. [6] limitation is set to a single trajectory analysis. Hussein et al. presented the time dependant stress and temperature results of the whole simulations, this thesis will compare the results to the first scanning track.

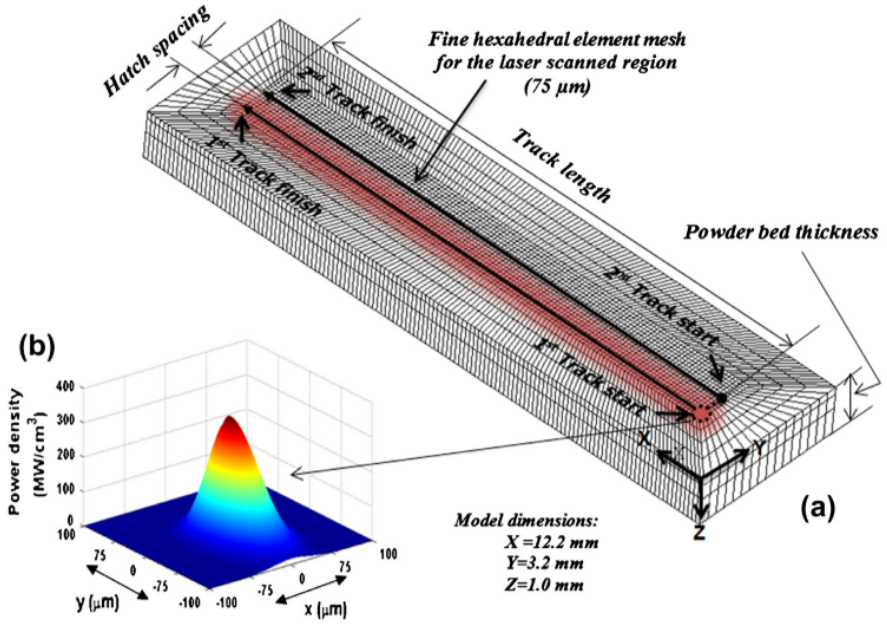

Figure 3.2: The model setup as presented in Hussein et al. [6].

Process parameter	value
Laser power, P $[W]$	100
Laser spot size, r_0 $[mm]$	0.075
Layer thickness, $[mm]$	1
Scanning speed, V $[mm/s]$	100
Track length $[mm]$	10
Absorption rate of powder from eq. (2.7), A $[-]$	0.3
Initial temperature, T_0 [°C]	26.85

Table 3.2: Simulation parameters used in Hussein et al. [6] and the thermo-mechanical simulation in this thesis.

3.1.1 Single track transient thermal analysis

3.1.1.1 Domain and meshing

The domain of the simulation is a 6x1.2x1mm bock of powder split into 120x30x12 elements as is shown on figure 3.3. In AdditiveLab, meshing is periodically performed using a built-in function. The domain dimensions and number of elements per dimension are specified, the function then sets the dimensions elements sized by a growth factor to be smallest at the top center and larger towards the lower side and edges. The simulations in this thesis are single trajectory scanning path analysis so thermal buildup where the powder temperature rises across multiple laser passes is not a concern. The trajectory is increased to 5mm to ensure a melt-pool steady state in achieved. The spot radius is 0.3mm and scanning path is 5mm, the domain has to be larger than the scanned area to account for the surrounding powder in the heat affected area and avoid boundary effect while it should not be excessively

large to limit computational cost. A 0.3mm border region outside of the laser spot is chosen for the sides, and a 0.2mm for the length dimension.

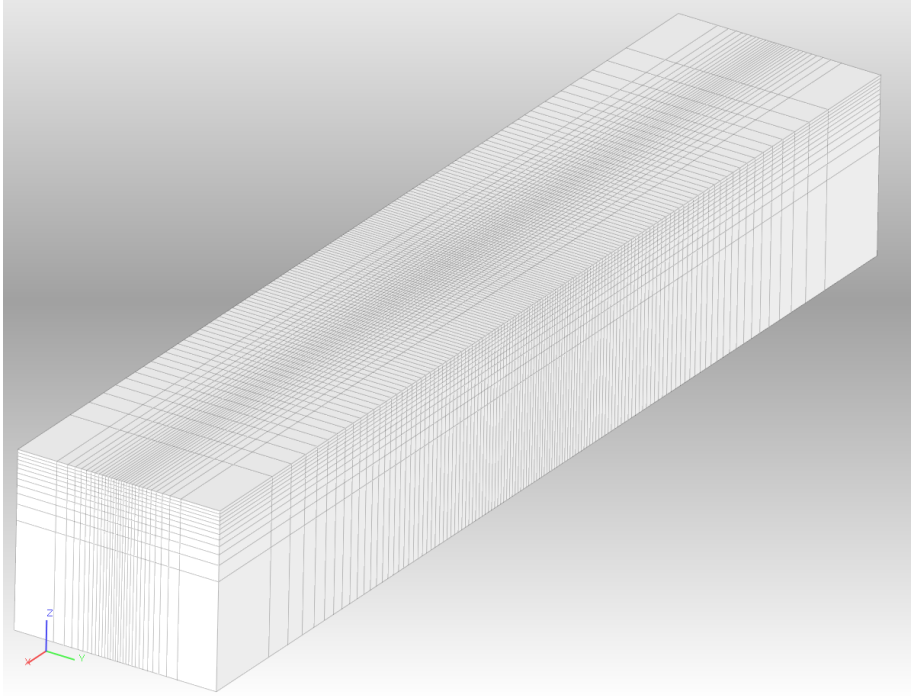

Figure 3.3: Picture of the mesh used, note that the elements are progressively smaller as they approach the center x: 6mm, y:1.2mm and z:1mm

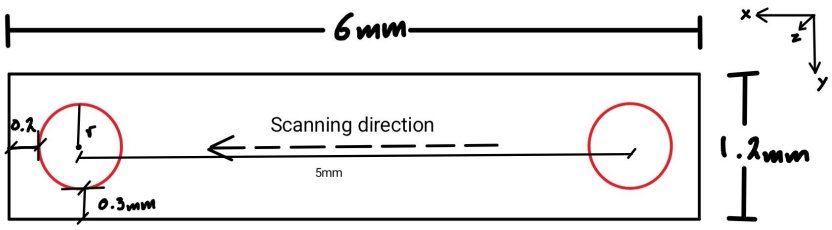

Figure 3.4: Schematic figure of the scanning track of the transient thermal simulation

3.1.1.2 Boundary conditions (thermal)

In AdditiveLab all sides of the domain have a convection boundary condition, while the top layer has a convection and radiation boundary condition, they are shown in figure 3.6 and clarified in tables 3.4 and 3.3.

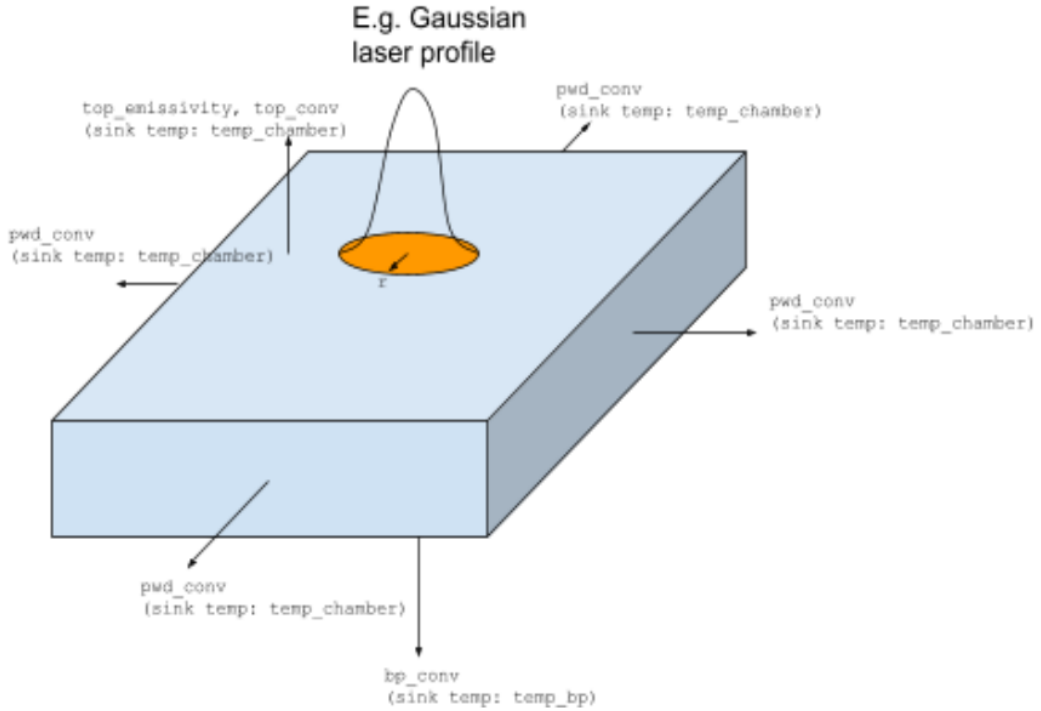

Figure 3.5: Picture of how AdditiveLab applies boundary conditions.From AdditiveLab users manual V5

Variable	Definition	Unit
top_conv	Convection Coefficient of top layer ($h_{\Gamma 2}$)	$[W/m^2k]$
pwd_conv	Convection Coefficient of sides ($h_{\Gamma 1,1}$)	$[W/m^2k]$
bp_conv	Convection Coefficient of bottom layer ($h_{\Gamma 1,2}$)	$[W/m^2k]$
temp_pb	Build plate temperature ($T_{amb,bp}$)	[°C]
temp_chamber	Build chamber air temperature (T_{amb})	[°C]
top_emissivity	Surface emissivity (ϵ)	$[-]$

Table 3.3: table relating the variables on figure 3.5 to bpundary conditions as described in figure 2.2

Boundary Condition	implementation
Convection top layer (2.3)	$q_{conv,\Gamma 2} = h_{\Gamma 2} \cdot (T - T_{amb})$
Radiation top layer (2.4)	$q_{rad,\Gamma 2} = \epsilon \cdot \sigma_r \cdot ((T + 273.15)^4 - (T_{amb} + 273.15)^4)$
Convection Sides (2.3)	$q_{conv,\Gamma 1,1} = h_{\Gamma 1,1} \cdot (T - T_{amb})$
Convection bottom (2.3)	$q_{conv,\Gamma 1,2} = h_{\Gamma 1,2} \cdot (T - T_{amb,bp})$

Table 3.4: Implementation of boundary conditions in AdditiveLab. where σ_r is the Stefan Boltzman constant, $\sigma_r = 5.67 \cdot 10^{-}8W/m^2K^4$. T is the surface temperature at the relevant boundary [°C].

Initial temperature is set as 20°C at $t = 0$ on in the powder. Emissivity will be $\epsilon = 0$ for the validation of the simulations. Becker et al. [24] proposed emissivity of $\epsilon = 0.55 - 0.65$ for a 1mm thick powder layer. The two extreme values will be used to test the sensitivity of this boundary condition. Since the powder layer is has great thickness, heat transfer to the bottom is considered negligible and the bottom layer convection coefficient is taken as 0. The side powder-powder boundary convection coefficient is taken as $0.001 mW/mm^2K$ (milliwatts per square millimeter kelvin), or a tenth of the top layer, to account for the powder being insulating. The values taken for the boundary conditions are shown in tables 3.5 and 3.6

Variable	value	Unit
convection coefficient of the sides ($h_{\Gamma 1,1}$)	1	$[W/m^2k]$
convection coefficient for the bottom layer ($h_{\Gamma 1,2}$)	0	$[W/m^2k]$
temperature of the build plate ($T_{amb,bp}$)	20	[°C]
air temperature in the build chamber (T_{amb})	20	[°C]

Table 3.5: Values for boundary conditions taken in all transient thermal simulations in this thesis

Boundary Condition	1	2	3
top layer convection coefficient ($h_{\Gamma 2}$) $[W/m^2k]$	10	10	10
top layer emissivity coefficient (ϵ) $[-]$	0	0.55	0.65

Table 3.6: Boundary conditions for $\Gamma 2$ for each transient thermal simulation

3.1.1.3 Heat source model

In Foroozmehr et al. [5] a volumetric heat source with a uniform distribution in the plane and a Gaussian distribution in the depth direction. Here a volumetric heat source with a Gaussian distribution in the x-y plane and a uniform distribution in the z-direction as is described in eq. (2.8) is used. Using the same spot diameter, laser power, absorption rate and optical penetration depth will result in the same energy density (J/mm^3, joules per cubic millimeter). Huang et al. [25] found that using different heat source models with the same energy density could yield comparable results.
The Rod gaussian distribution: The heat load is distributed according a Gaussian curve within the radius of the spot, and uniformly distributed down to the laser penetration depth.

$$Q(r,z) = SfactQ_0 e^{-Sfact(\frac{r}{r_0})^2} \tag{3.1}$$

where:
$Sfact$ is the dimensionless shape factor $[-]$
r is the distance from the center of the spot $[mm]$

r_0 is the spot radius $[mm]$

α is the absorption coefficient $[-]$

Q_0 is the peak volumetric heat flux, described in equation (3.2) $[mW/(mm^3)]$

$$Q_0 = \frac{PA}{r_0 \pi^2 d} \tag{3.2}$$

where:

P is the laser power $[mW]$

r_0 is the spot radius $[mm]$

A is the absorption coefficient $[-]$

d is the optical penetration depth $[mm]$

It should be noted that the energy delivered is dependent on the shape factor, this effect can be quantified

$$Q = \int_V Sfact * q_{v0} e^{-Sfact*(\frac{r}{r_0})^2} \, dV \tag{3.3}$$

$$= \int_0^d \int_0^{r_0} \int_0^{2\pi} Sfact * q_{v0} * e^{-Sfact*(\frac{r}{r_0})^2} \, r d\theta dr dz$$

$$= 2\pi d Sfact q_{v0} \int_0^{r_0} e^{-Sfact*(\frac{r}{r_0})^2} \, r dr$$

$$= \pi d r_0^2 q_{v0} (1 - e^{-Sfact})$$

From the definition of q_{b0} we get the energy delivered is $Q = P * A * (1 - e^{-Sfact})$ instead of the expected $Q = P * A$. For the most commonly used value of $Sfact = 2$ this equates to around 14% reduction in power delivered to the system.

3.1.1.4 Material parameters

Material parameters for the thermal properties are presesented in this section. The powder conductivity is modelled as 0.01 of conductivity of the solid metal. table 3.7 shows the temperature dependent density, conductivity and specific heat data for 316L steel used in the simulations in this thesis.

Temperature (T) [°C]	Density (ρ) [kg/m^3]	Conductivity (k_{solid}) [W/mK]	Specific Heat (C_p) [J/kgK]
25	7990	13.67	447
100	7960	14.67	468
200	7920	16.00	489
300	7870	17.34	507
400	7820	18.68	524
500	7770	20.01	540
600	7730	21.35	557
700	7680	22.69	574
800	7630	24.02	592
900	7580	25.36	610
1000	7530	26.69	628
1100	7480	28.03	648
1200	7430	29.36	668
1300	7370	30.7	688
1400	7320	32.28	852
1422		32.793	
1556			858.17
2754	6012		

Table 3.7: Temperature dependent density, conductivity and specific heat data for powder and solid 316L steel used in AdditiveLab simulations

Foroozmehr et al.[5] used values for solid 316L material properties recommended by Mills [28] shown in table 3.8

Temperature (T) (deg C)	**Density (ρ)** (kg/m^3)	**specific heat (C_p)** (J/gK)	**conductivity (k)** (W/mK)
25	7950	0.47	13.4
100	7921	0.49	15.5
200	7880	0.52	17.6
300	7833	0.54	19.4
400	7785	0.56	21.8
500	7735	0.57	23.4
600	7681	0.59	24.5
700	7628	0.60	25.1
800	7575	0.63	27.2
900	7520	0.64	27.9
1000	7462	0.66	29.1
1100	7411	0.67	29.3
1200	7361	0.70	30.9
1300	7311	0.71	31.1
1385	7269	0.72	
1450	7236	0.73	28.5
1450	6881	0.83	28.5
1600	6765	0.83	30.5

Table 3.8: Recommended values for thermophysical properties of 316 stainless steel from Mills table 1 on page 142 [28]. Data in this table is used in Foroozmehr's et al [5] not in the simulations in this thesis.

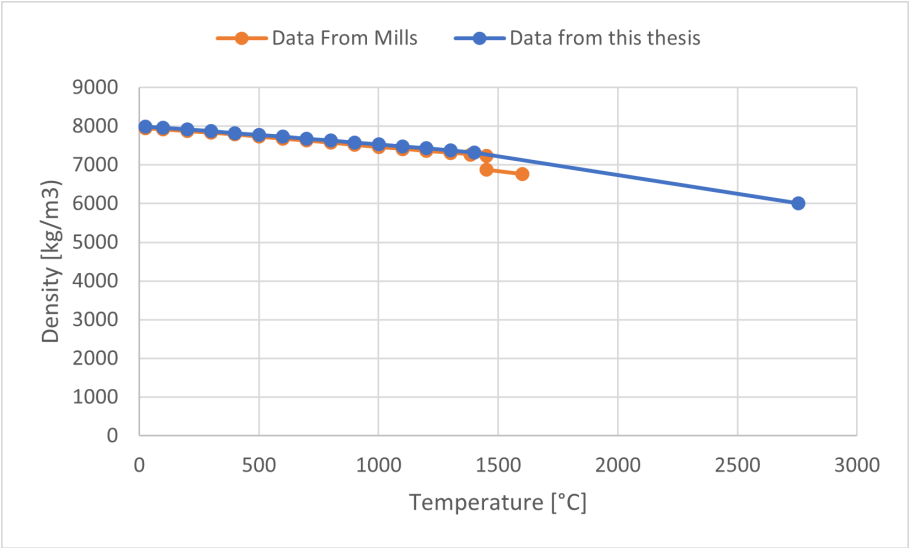

Figure 3.6: Graph of temperature dependent density data for powder and solid 316L steel used in AdditiveLab simulations shown with values reccomended by Mills [28]

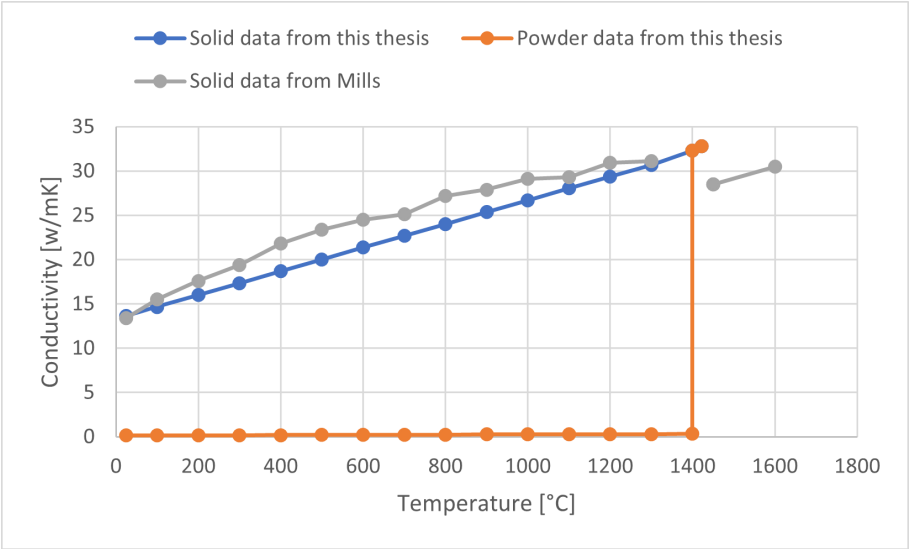

Figure 3.7: Graph of temperature dependant conductivity data for 316L steel used in simulations using AdditiveLabshown with data reccomended by Mills [28]. Abrupt change in conductivity is from the phase change model in AdditiveLab, the conductivity of powder is modelled as 0.01% of solid metal before it reaches melting temperature.

AdditiveLab uses a phase change model that assumes the density and specific heat of powder is the same as the bulk material. The stiffness (E), conductivity (k) and thermal expansion coefficient (α) are then modelled as a constant fraction of the bulk properties. At the start of the simulation, k, E and alpha are scaled with $k_{powder} = 0.01k_{solid}$, $E_{powder} = 0.001E_{solid}$ and $\alpha_{powder} = 0.0 \cdot \alpha_{solid}$. These coefficients are then changed to 1.0 at the melting temperature of T=1399°C. Once the material has been melted it can never go back to powder [27].

Table 3.7 and figure 3.8 show the specific heat data for both the solid and powder. In AdditiveLab latent heat in fusion is not modelled explicitly, the heat capacity (C_p) is the temperature derivative of the enthalpy (H), so the effect from the latent heat is captured as an increase in the specific heat at the temperature where phase change occurs using apparent heat capacity [21].

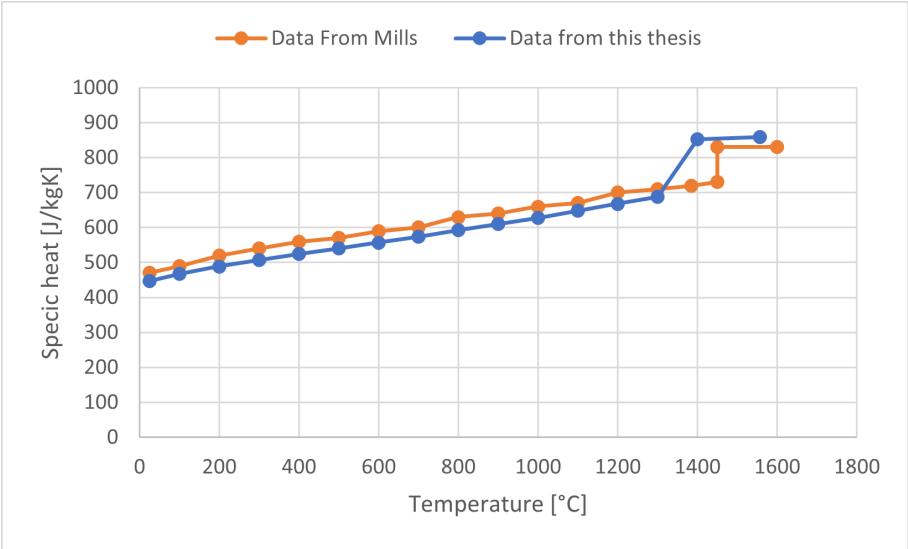

Figure 3.8: Specific heat of powder and steel parameters used for Simulations in AdditiveLab shown with values reccomended by Mills [28]. Note an increase in specific heat at the melting temperature

3.1.2 Single track thermo-mechanical analysis

3.1.2.1 Domain and meshing

For the thermomechanical simulation, the mesh is built with the same function as in the transient thermal simulation. The domain must be larger than the scanned area to account for the surrounding powder in the heat-affected zone and to avoid boundary effects. The spot diameter is 0.15mm, so a domain of 12x1.2x1 is chosen to provide border of 1mm on either end and 0.5mm on the sides.

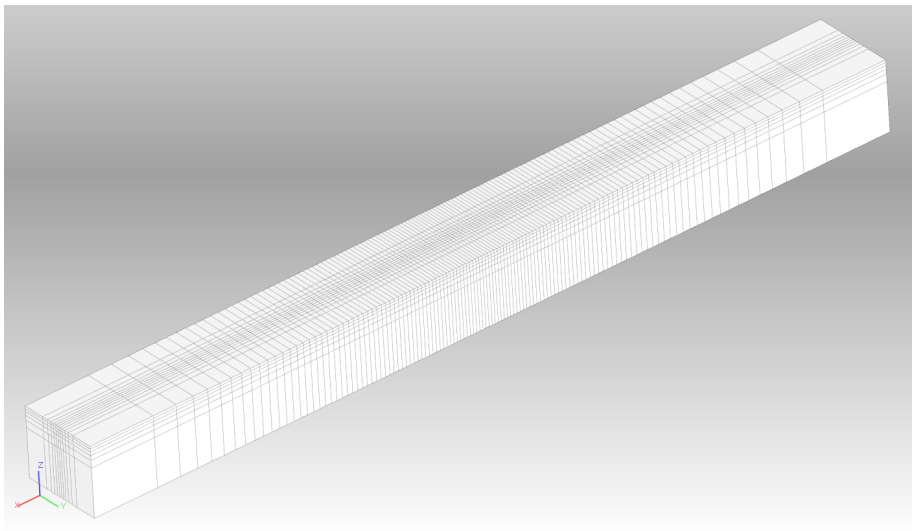

Figure 3.9: The mesh used in thermo-mechanical simulations

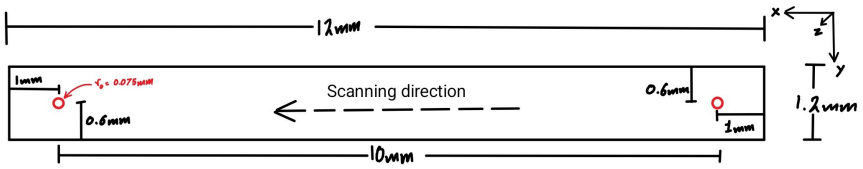

Figure 3.10: A schematic figure of the scanning track used in the thermomechanical simulation

3.1.2.2 Boundary conditions

The Thermal boundary conditions in the thermo-mechanical simulation are the same as in the transient thermal simulation. They are described in table 3.9.

Variable	Variable	value	Unit
Sides convection coefficient (h_{pow})	0.001	$[mW/mm^2k]$	
Bottom layer convection coefficient (h_{bp})	0	$[mW/mm^2k]$	
Bottom layer ambient temperature (T_{amb})	20	[°C]	
Ambient air temperature of the chamber (T_{amb})	20	[°C]	
Top layer convection coefficient (h_{rad})	0.01	$[mW/mm^2k]$	
Top layer emissivity coefficient (ϵ)	0.0	[−]	

Table 3.9: Parameters for thermal boundary conditions

The heat source is surface Gaussian as presented in (2.7). With P=100W, A=0.3 and r_0=0.075mm. And scanning speed V=100mm/s.
The mechanical boundary conditions, fixed on the bottom free on the top and gliding on the sides.

3.1.2.3 Material parameters

The thermal parameters are the same as in the transient thermal simulation. The mechanical material parameters for the bulk material are presented in table 3.10, as well as a Poisson's ratio of ν=0.3.

Temperature (T)	$[°C]$	25	200	400	600	700	800	1300
Coefficient of thermal expansion (α)	[-]	14.3	15.6	16.9	17.7	18.5	19.1	19.5
Modulus of elasticity (E)	[GPa]	198.5	187	172	157	141	106	10
Yield strength (f_y)	[MPa]	282	217	161	153	108	50	5

Table 3.10: Temperature dependent mechanical parameters for mechanical properties from Hussein et al. [6]

The material parameters for the powder are the same as for the bulk material, except for the modulus of elasticity (E) and thermal expansion coefficient α. They are multiplied with scaling coefficients 0.001 and 0 respectively. When the powder reaches the melting temperature, the scaling coefficients are changed to 1.

4

Results

In this chapter, the outcomes of the thermal and thermo-mechanical simulations are presented and analyzed. The results focus on key metrics such as thermal distribution, melt-pool dimensions, and the development of residual stresses. By comparing these results with experimental data, accuracy of the simulations using AdditiveLab are evaluated.

4.1 Transient thermal results

The first validation experiment is to see how AdditiveLab scanning path simulations compare to the reference simulations from Foroosmehr et al. [5].

The exact position or time measurements in Foroozmehr's data is not stated, the best comparison is to the middle and end of the track, once the melt pool has reached a steady state. During the fist 3 simulations from table 4.1 in AdditiveLab, initially the maximum temperature of the simulation domain rises until some maximum value of around 2020°C, then it remains stable at around 2000°C until the spot reaches the end of the scanning track. Point 1 is chosen as a spot on the track after the maximum temperature is reached near the start of the track to observe a longer cooling history. Point 1 is at coordinate x=2.09mm, 1.34mm from the start of the scanning path. Where the maximum temperature in the simulation had reached it's peak value, shown on figure 4.1.

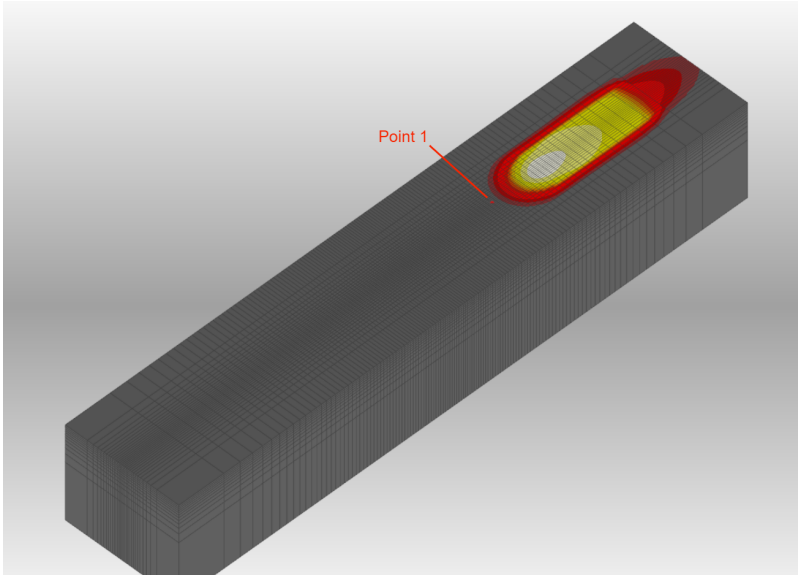

Figure 4.1: Position of point 1 for laser speed 100mm/s

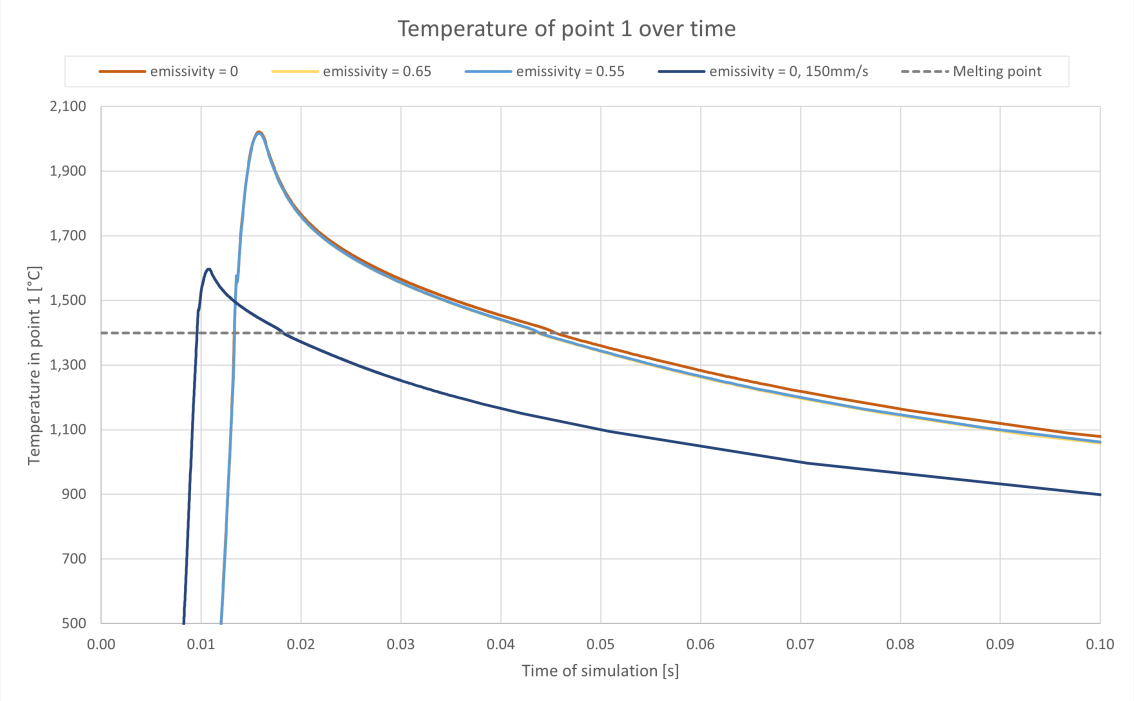

Figure 4.2: Graph of temperature at point 1 over time for different values of scan speed and emissivity

The melt-pool is defined as the volume of the simulation domain with temperature elevated above the melting temperature. Its dimensions are determined by a script native to AdditiveLab [4] shown in Appendix 4. For each time-step, the nodes that are above the melting temperature of 1339°C are collected and the dimensions bound by them are marked as the melt-pool depth, width, and length. Instead of comparing the length of the melt-pool, the length of time that a single point remains

Scan speed (V) [mm/s]	Emissivity (ϵ) [-]	Max temperature [°C]	Liquid lifetime [ms]	Depth [mm]	Width [mm]
100	0	2021	32.0	0.1153	0.4102
100	0.55	2017	30.6	0.1153	0.4097
100	0.65	2016	30.3	0.1153	0.4097
150	0	1597	8.66	0.1067	0.2539

Table 4.1: Melt-pool temperature and dimensions from the simulations using AdditiveLab

Scanning Path Points	Start of track	Middle point	End point
Depth [mm]	0.120	0.155	0.155
Width [mm]	0.440	0.440	0.500
Length [mm]	0.500	0.800	0.800

Table 4.2: Melt-pool dimentions from Foroozmehr's et al. [5] scanning path simulations

above the melting temperature called liquid lifetime of the melt pool is compared. In steady state condtions the length of the melt pool determines the liquid lifetime of the melt-pool, as the length of the melt-pool divided by the scanning speed is the time that a single point remains above the melting temperature.
Defining the difference of the results as the difference between the values divided by their mean value, expressed as:

$$\frac{|value_1 - value_2|}{(value_1 + value_2)/2}$$

Comparing the results of the first simulation from table 4.1, with scanning speed $V = 100mm/s$ and emissivity $\epsilon = o$ to Foroozmehr's results in table 4.3, the simulation using AdditiveLab has a shallower and thinner melt-pool, with a depth difference of 25.6%, the width a difference of 6.8% in the middle of the track and 17.9% at the end of the track. The length of the melt-pool in Foroozmehr et al. [5] corresponds to about 8ms lifetime, a 300% difference compared to the 32ms from the simulation using AdditiveLab.

Simulation	Depth [μm]	Width [μm]	Liquid life time [ms]
Thesis simulation	115	410	32
Foroozmehr et al.	155	440	8ms

Table 4.3: Melt-pool dimentions from Foroozmehr et al. [5] compared to the simulation in this thesis

4.1.1 Discussions of transient thermal simulation results

There are a number of differences in the simulations that could cause the difference in results. To start off, the heat source model uses a different distribution. as discussed in 3.1.1.3 Foroozmehr et al. [5] used a heat source that was evenly distributed in the x-y plane and with a Gaussian distribution in the z-dimension, while the heat source in this thesis has a Gaussian distribution in the x-y plane and is evenly distributed in the z-dimension. This results in the heat input in Foroozmehr et al. [5] to be more concentrated near the surface compared to the simulation in this thesis. However, in Foroozmehr's et al. [5] the melt-pool depth is greater than the optical penetration depth (defined in eq. (2.8)) $OPD = 120\mu m$, while the depth in the simulation using AdditiveLab is lesser than the OPD. There is no heat source below the optical penetration depth, so the portion of the melt-pool that is deeper than OPD in Foroozmehr's simulation is heated only with conductive heat transfer while all of the melt-pool in the simulation using AdditiveLab was withing the boundaries of the heat source. This suggest that differences in conductive heat transfer is the main cause for the difference in results rather than the heat source model. First, to compare the input data. Foroozmehr et al.[5] used values for solid 316L material properties recommended by Mills [28] shown in table 3.8. The conductivity is not significantly different than the values used in AdditiveLab with powder having 1% of the conductivity of the solid in both simulations.
The data for the temperature dependent specific heat and conductivity in table 3.7 do not reach the maximum temperature in the simulation, AdditiveLab simulations take the value of the highest given temperature dependant value, when the temperature of the material exceeds it. While Foroozmehr et al. [5] added extreme temperature values to the material data to linearly extrapolate the values from table 3.8 recommended by Mills [28]
Foroozmehr et al. [5] model latent heat in fusion directly while the simulations in AdditiveLab used apparent heat capacity included in the material parameters to account for the latent heat in fusion. However differences in latent heat have been shown to not greatly impact the melt-pool temperature field or dimensions [15].
Likely the largest difference is due to the differences in phase change model. AdditiveLab models powder as having the same density and specific heat as solid metal, changing only the conductivity of the powder from 0.01 times the conductivity of the solid proprety in table 3.7 at the melting temperature. This will have an effect on the temperature distribution in the powder and results in a different shape of the melt-pool. According to Foroozmehr et al. [5], the heat capacity of powder is almost equal to the heat capacity of solid metal. This is true when measuring the heat capacity per unit mass, as the gas phase of the powder is a small fraction of the mass of the powder. however, the heat capacity per unit volume is drastically different. This model overestimates the volumetric heat capacity of the powder and slows down the heat conduction to the surrounding powder. Figure 4.3 shows the volumetric heat capacity in the powder using the phase change model from Foroozmehr et al. [5] compared to the material data for the AdditiveLab analysis.
Foroozmehr used 40% powder porosity, compared to the simulations in Additive Lab, where the density of powder is the same as solid metal, or corresponding to 0% porosity. Criales et al.[15] found that melt pool geometry (depth, width and length)

is sensitive to the packing density of powder. Where a decrease of porosity in the powder from 30% to 10% corresponded to around 2% lesser maximum heat, 10% longer life-time of the melt-pool, and around 8% reduction in width. The difference between the powder density in Foroozmehr et al. [5] and the simulations in this thesis is much larger than the variation of powder density in Criales et al. [15]. This large discrepancy between the models is likely a major cause of the differences between the simulation results in this thesis and Foroozmehr et al. [5].

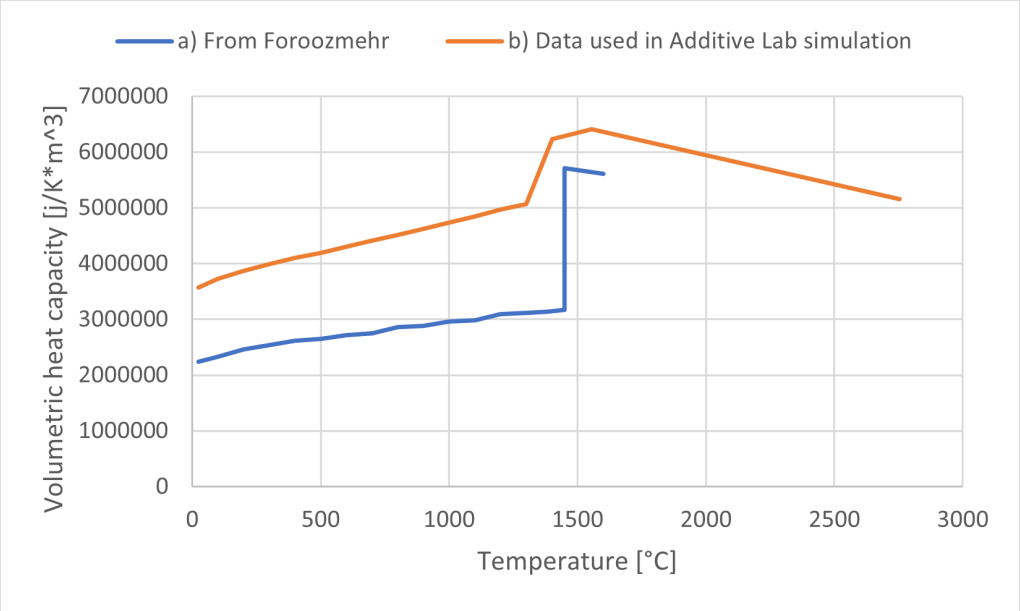

Figure 4.3: Volumetric heat capacity vs temperature, a) using the powder model described in Foroozmehr et al. and b) using the powder material model in AdditiveLab

Effect of variations in emissivity: including the radiation boundary condition($\epsilon = 0.65$) caused the liquid lifetime of the melt-pool lower from 32.0 ms at $\epsilon = 0$ to 30.3 ms with $\epsilon = 0.65$. This indicates that higher emissivity results in a shorter duration that point 1 stays above the melting temperature to a small degree. The depth remains constant at 0.1153 mm regardless of the emissivity. This shows that the depth of the melt pool is not significantly affected by changes in emissivity within the range tested. Similar to the depth, the change in width is minimal, suggesting that the width of the melt pool is relatively insensitive to emissivity variations within this range at these temperatures. This analysis suggests that while emissivity influences the thermal aspects of the melt pool (temperature and lifetime), it has a negligible effect on the geometrical dimensions (depth and width) of the melt pool in the PBF-LB process for 316L steel. This indicates that the radiation boundary condition for calibrated transient thermal process simulations can be omitted without much loss of accuracy.

4.2 Thermomechanical results

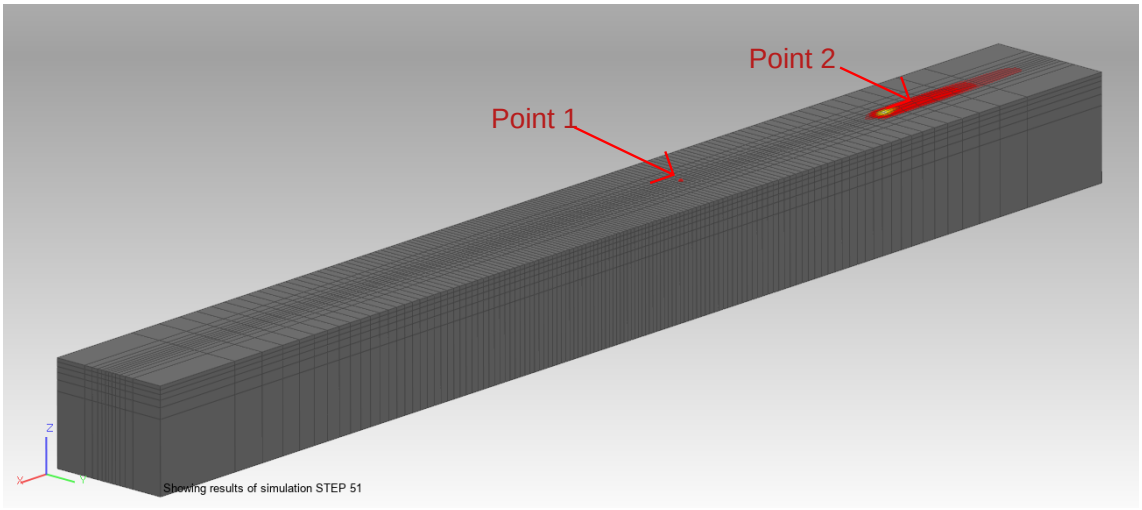

Figure 4.4: Position of points 1 and 2 in the simulation

Point 1 is near the middle of the track, there the elements are the smallest for the best accuracy of results. Hussein et al. [6] only presented results for the stress at the start of the tracks. This thesis studied point 1, as it has the finest mesh. However, stress development is different in at the middle of the track than it is at start. Point 2 has a much coarser mesh, and thus is of lesser interest in terms of the stress values, while the development of stress and relative magnitudes of the stress components are of interest.
The temperature distribution in figure 4.6 shows the temperature distribution along the track, though it has the same distribution as temperature over time after the melt-pool reaches a steady state. The temperature distribution in figure 4.5 shows a similar deviation from Hussein's results as the transient thermal analysis did from Foroozmehr's results. The peak temperature is 8200°C, much higher than Hussein's around 2500°C in figure 4.6. This temperature is much higher than evaporation temperature of around 3000°C. Evaporation is not included in this model and below this physically impossible result is taken as presented to study the development of residual stresses in simulations using AdditiveLab. The melt-pool cools down slower, with a melt-pool lifetime of 29.5ms compared to Hussein's 10ms.
Hussein only provides data melt-pool dimension data for the end of the 5th scanning track. However for a quick comparison, we can extrapolate from Foroozmehr's [5] results that the depth of the first track would be about half of the depth of the last track, as the depth of Foroozmehrs 3rd and 4th track are identical and almost twice the depth of the 1st track. The depth of the melt-pool 0.11mm compared to 0.6mm at the 5th track from Hussein et al [6]. This is a similar finding as in the transient thermal simulation and likely has the same cause. The melt-pool dimension results from Hussein with the dimensions from the simulation in this thesis are shown in table 4.4.
The strange temperature readings are likely due to the mesh being too course, as it

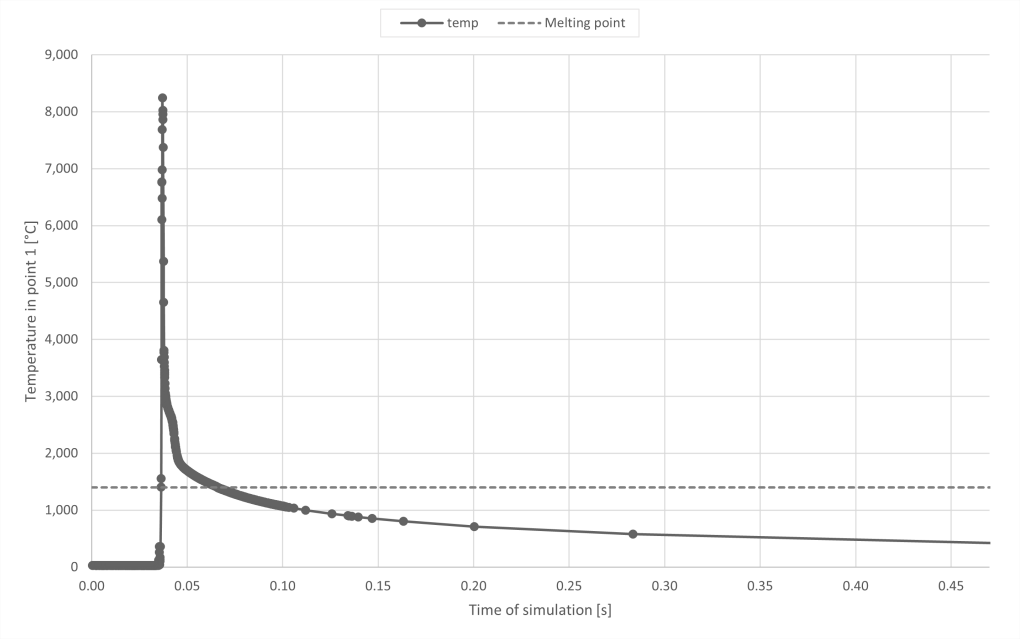

Figure 4.5: Temperature in point 1 in figure 4.4 over time.

Simulation	Depth [μm]	Width [μm]	Liquid life time [ms]
Thesis simulation	109	289	29.5
Hussein et al.	300	400	1mm

Table 4.4: Melt-pool dimentions from Hussein et al. [6] compared to the simulation in this thesis

to capture the heat distribution accurately. This problem is more pronounced with the surface heat source model as described by equation (2.7) as the beam intensity on the surface layer is higher than when using a the volumetric heat source described in (2.8). Consequently, the maximum temperature fluctuates between 6500°C and 8200°C, likely due to numerical concentration effects from the coarse mesh.

The temperature in figure 4.5 is higher than in figure 4.6, and cools down slower. However, the shape of the distribution is very similar. As the there is a twofold curve that the temperature gradient follows. There is no external load applied to the mechanical system, so thermal expansion acts as the only load on the mechanical simulation, consequently, variations in temperatures have a an effect on the displacement and stress distributions.

The Von Mises stress over time is shown in figure 4.7. As the material model reduces the stiffness to 10 GPa at the lowest as defined in table 3.10, the stress of the melt-pool is not zero.

The objective of this comparison is to investigate stress development in the simulation. The temperature in Hussein et al. [6] is 400°C at t=0.1s compared to around 1000°C in the simulation using AdditiveLab at the same time (t=0.1). As the stress development is a result of the temperature distribution, a comparison of the stress components at a point in time when the temperature in the simulation using Ad-

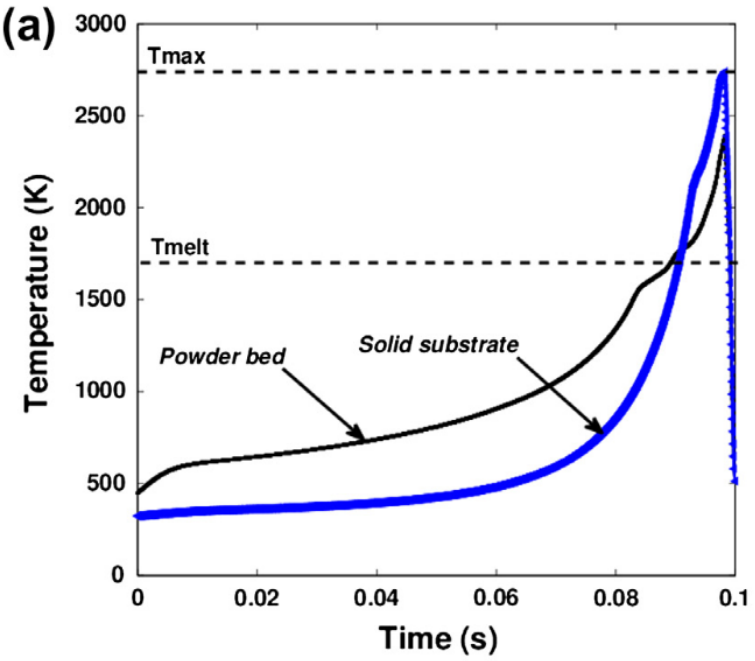

Figure 4.6: Surface temperature of powder-bed (Black line) along the track. Figure is from Hussein et al. [6], note that the horizontal axis is marked as time as a mistake, it should be marked as the position along the track from 0-10mm

ditiveLab lowers to 400°C is chosen instead. The temperature at point 1 lowers to 400°C at t=0.47s.
The maximum Von Mises stress is 159 MPa compared to 605 MPa in Hussein's simulation [6], this difference in results is to be expected as the cooling rate is slower in the simulation using AdditiveLab.
Looking into the different stress components: In Hussein's experiment, all stress components initially reach extreme tension values during the laser melting and the node compresses as it solidifies and cools down. In figure 4.8, the x and z components are in compression at the end of track one. Note that the sign convention is different in Hussein's simulation compared to AdditiveLab, in this thesis negative stress is compression.
As the laser approaches point 1 in figure 4.4, the stress values in the powder fluctuate between high compressive stress and high tensile stress. This is a numerical issue in the simulation and the values before melting are not included in the results in figure 4.9. Initially, A high tensile stress is formed as the laser melts the powder, really high uniform tensile stresses on the order of 1000 MPa are formed, the stress then lowers as the molten material settles until it solidifies. After solidification, the material continues to contract and both stiffness and yield strength increase, this results in a large tensile stresses as the material no longer yields at 5 MPa as prescribed in table 3.10. This highlights a flaw in the material parameters, as the liquid metal has elastic strain. At t=0.47, the x and y components are still tension, while the z component in compression. $\sigma_x = 43MPa$, $\sigma_y = 35MPa$, $\sigma_z = -120$.
Hussein was looking into a point at the start of the track. This thesis studied point 1, as it has the finest mesh. The stress development is different in at the middle

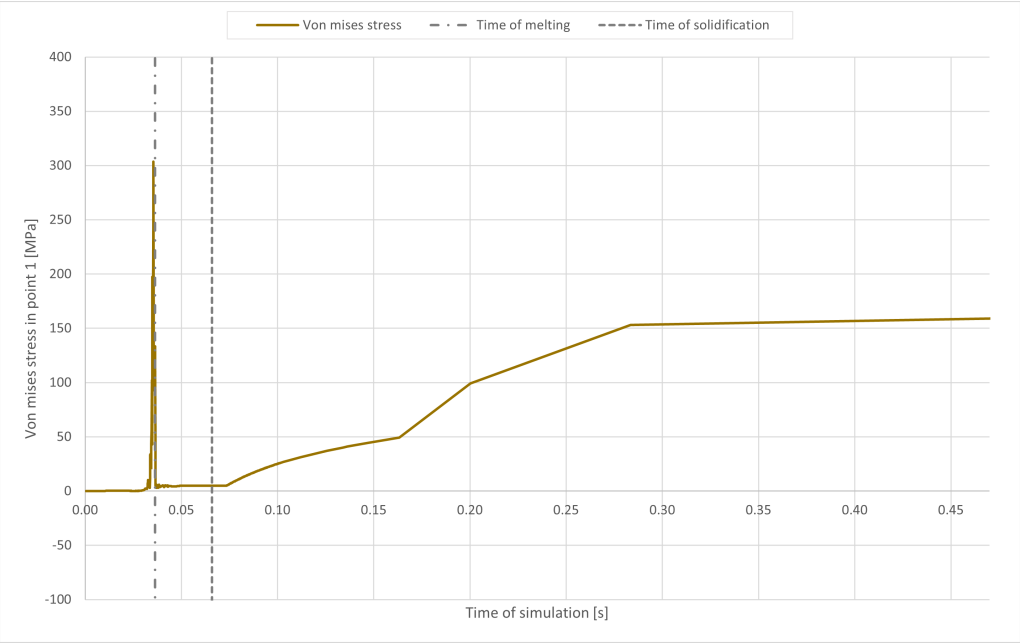

Figure 4.7: Von Mises stress in point 1 in figure 4.4 over time.

of the track than it is at start. Point 2 has a much coarser mesh, and thus is of lesser interest in terms of the stress values, the development of stress and relative magnitudes of the stress components are of interest. The Von Mises stress was 165 MPa at t=0.47 and all stress components are in compression as shown in figure 4.10. Comparing the simulation in this thesis to Hussein et al. [6]. The largest differences in the thermo-mechanical simulations are from the different temperature distribution as explored in transient thermal simulation chapter, and the plasticity model. The material parameters for temperature dependant yield strength from Hussein et al.[6] are implemented in the simulation in AdditiveLab.
While presenting temperature dependant yield strength, Hussein used an elastic simulation, the resulting Von Mises stress is much higher than the yield strength, as the strains are so high.
In the simulations using AdditiveLab, there is an initial sharp rise in stress before melting, when it reaches the melting point, the modulus of elasticity and expansion of coefficient scaling coefficients change from 0.001 and 0.0 respectively to 1. The material yields and the stresses relax. As the material cools down, the strength and stiffness increase as per table 3.10 and tensile stresses increase. As cooling continues they turn into compressive stresses. The differences between point one and 2 are due to the position in the track, as there is less over all stress at the position. Both points are at the middle surface of the track, and thus show a very similar stress component development as the material cools. In figure 4.11 the Von Mises stresses of points 1 and 2 are compared over time, the longer since the point solidified, difference in stress decreases.

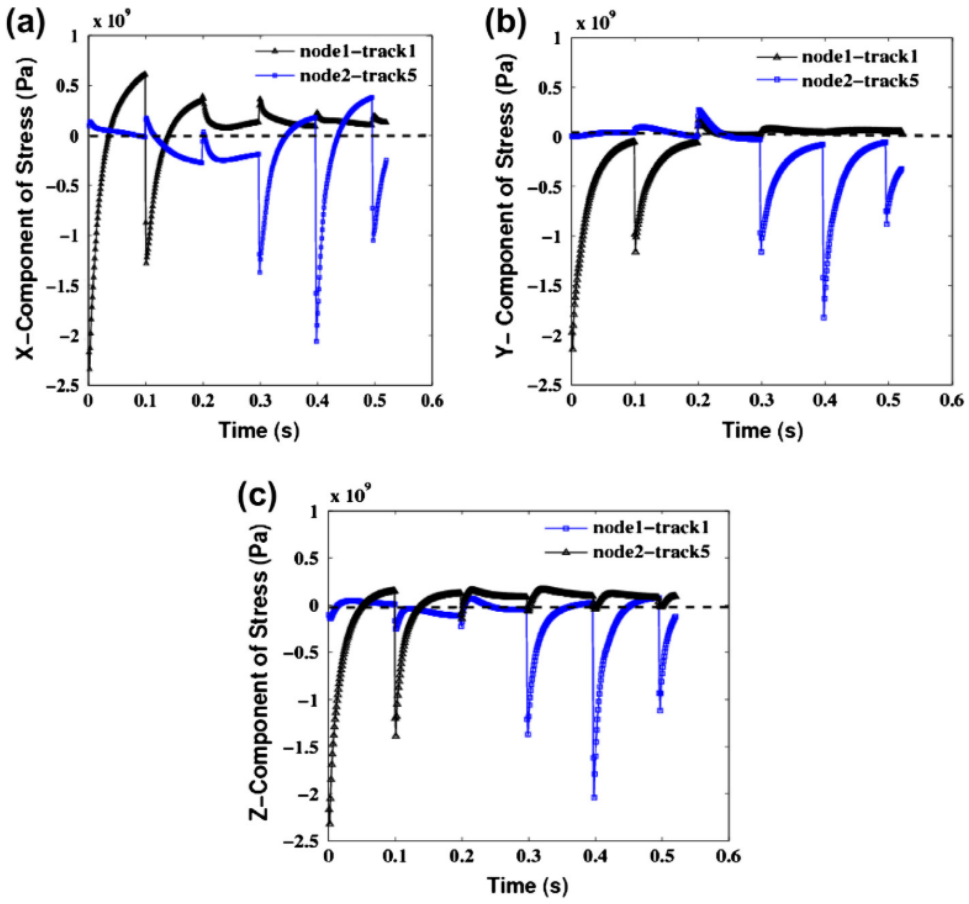

Figure 4.8: Cartesian normal stress components from Hussein et al. x is along the scan direction, y is transverse to the scanning direction along the width, and z is transverse along the depth.

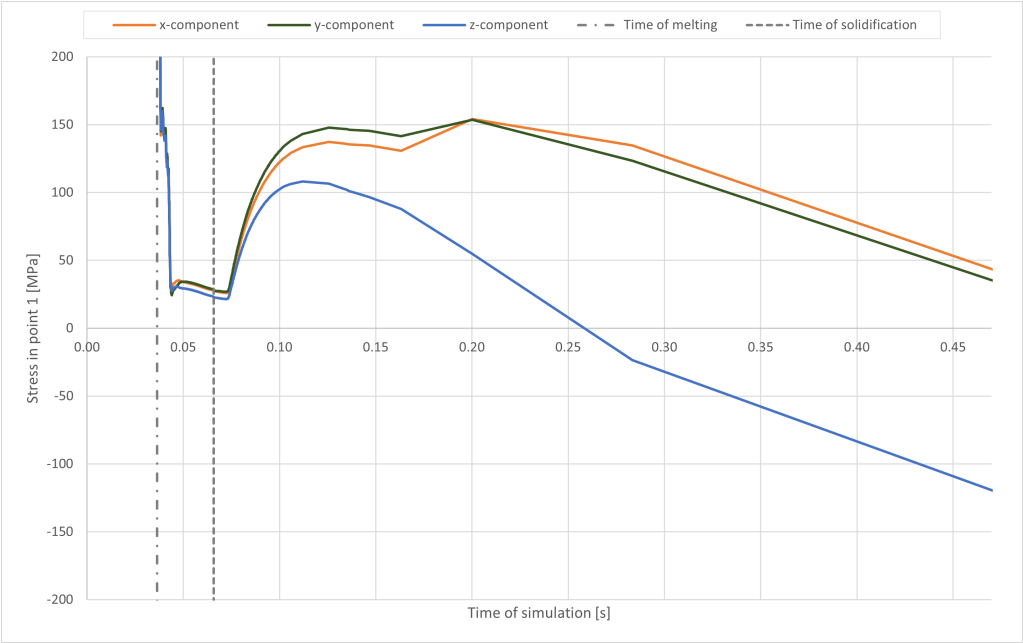

Figure 4.9: Normal stress components in point 1 over time.

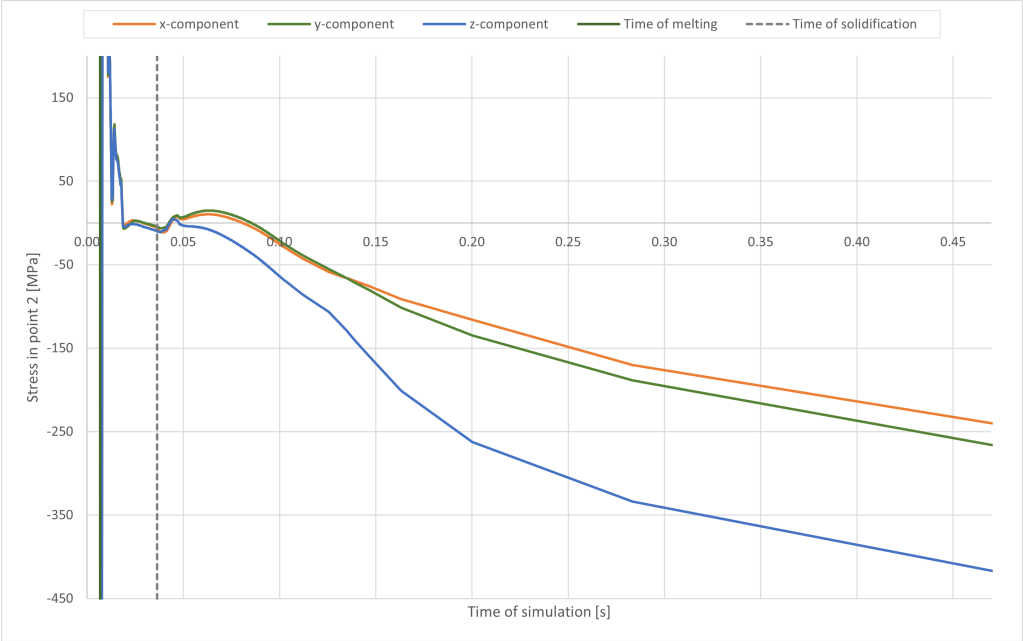

Figure 4.10: Normal stress components in point 2 introduced in figure 4.4 over time.

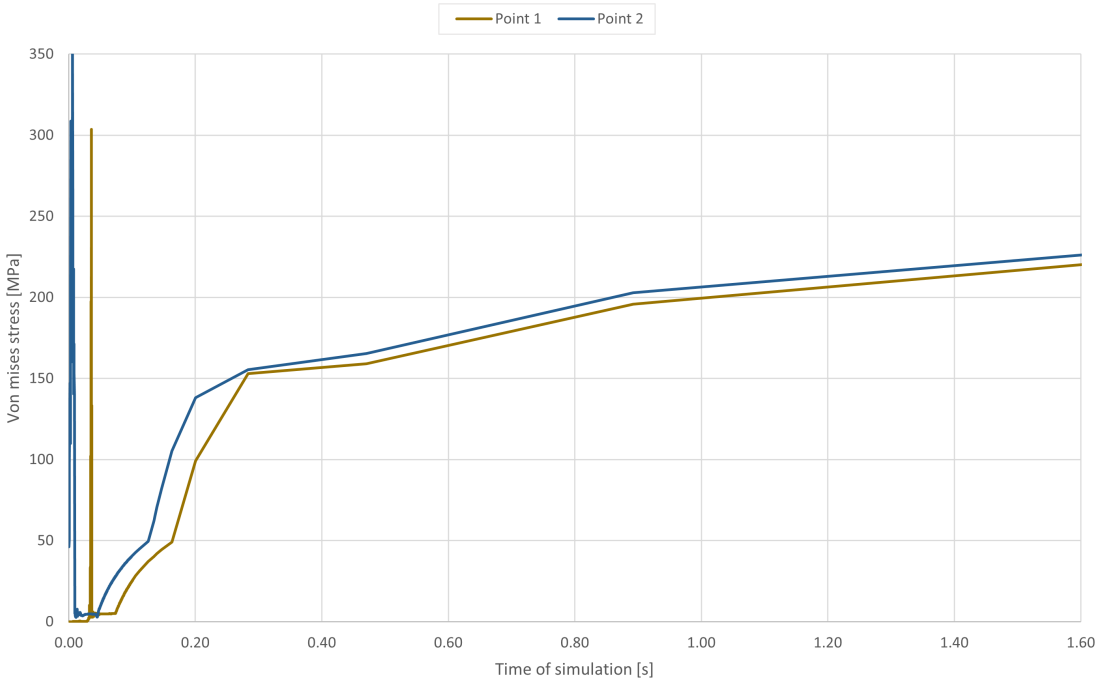

Figure 4.11: Von Mises stress in points 1 (brown) and 2 (blue) introduced in figure 4.4 over time

5
Conclusion

AdditiveLab provides a functional tool for meso-scale process simulation in PBFLB; however, it does have some limitations. The simplified phase-change model used in AdditiveLab results in differences in temperature distribution. Modeling powder as having the same density and specific heat as bulk material leads to a different temperature distribution, an underestimation of melt-pool depth, and an overestimation of the lifetime.
Other studies have claimed that the heat capacity of the powder and the bulk material is very similar, however the density of the powder and thus the volumetric heat capacity ($\rho \cdot C_p$) of powder is much lower. Including this difference in density is important to accurately capture the temperature distribution. Including plasticity in the simulations is important in simulating the formation of residual stresses.
The results showed significant differences in the stress development compared to purely elastic simulations. The elastic simulation ended with elevated temperatures; if it were to cool down to the initial temperature, all of the material would return to the original volume and no residual stresses would remain.
Due to time limitations, there was not a sufficiently good mesh convergence study performed on the scanning path simulations in AdditiveLab version 5, so effects like the stress concentrations in the powder just before melting is an artifact of the meshing and time-stepping of the simulation. PBF-LB simulations are highly nonlinear and very computationally heavy, with thermo-mechanical simulations generally taking hours or even days to run. A further study of the effects of element size and time increments is needed to properly assess the effect they played on the results in this thesis. Additional simulations using a general solver such as Ansys or Abaqus with a phase-change model that includes the density difference of bulk material are proposed for future work. The additional simulations should also account for the sensitivity of the PBF-LB process to variations in the volumetric heat capacity.

Bibliography

[1] Strondl, A.& Uhlirsch, M., Karlsson, S., Hallberg, P. & Widfeldt, M., Hryha, E.& Nyborg, L., Lindgren, A., Lindwall, G., FuRAM – Follow-up on research needs for industrialization of metal additive manufacturing. *Swerim ab*, MEF21192, (2021,08)

[2] Chowdhury, S., Yadaiah, N., Prakash, C., Ramakrishna, S., Dixit, S., Gupta, L. & Buddhi, D. Laser powder bed fusion: a state-of-the-art review of the technology, materials, properties & defects, and numerical modelling. *J. Mater. Res. Technol.*. **20** pp. 2109-2172 (2022,9)

[3] Bayat, M., Dong, W., Thorborg, J., To, A. & Hattel, J. A review of multi-scale and multi-physics simulations of metal additive manufacturing processes with focus on modeling strategies. *Addit. Manuf.*. **47**, 102278 (2021,11)

[4] "Additive Lab research", Additive-lab.com, (2024.7), https://www.additive-lab.com/additivelabresearch

[5] Foroozmehr, A., Badrossamay, M., Foroozmehr, E. & Golabi, S. Finite Element Simulation of Selective Laser Melting process considering Optical Penetration Depth of laser in powder bed. *Mater. Des.*. **89** pp. 255-263 (2016,1)

[6] Hussein, A., Hao, L., Yan, C. & Everson, R. Finite element simulation of the temperature and stress fields in single layers built without-support in selective laser melting. *Mater. Eng.*. **52** pp. 638-647 (2013,12)

[7] Zhang, X. Modeling and analysis of modern fluid problems. (Academic Press,2017,4)

[8] Oliveira, J., LaLonde, A. & Ma, J. Processing parameters in laser powder bed fusion metal additive manufacturing. *Mater. Des.*. **193**, 108762 (2020,8)

[9] Liu, J. & Wen, P. Metal vaporization and its influence during laser powder bed fusion process. *Mater. Des.*. **215**, 110505 (2022,3)

[10] Young, Z., Guo, Q., Parab, N., Zhao, C., Qu, M., Escano, L., Fezzaa, K., Everhart, W., Sun, T. & Chen, L. Types of spatter and their features and formation mechanisms in laser powder bed fusion additive manufacturing process. *Addit. Manuf.*. **36**, 101438 (2020,12)

[11] Patel, S. & Vlasea, M. Melting modes in laser powder bed fusion. *Materialia*. **9**, 100591 (2020,3)

[12] Tolochko, N., Khlopkov, Y., Mozzharov, S., Ignatiev, M., Laoui, T. & Titov, V. Absorptance of powder materials suitable for laser sintering. *Rapid Prototyp. J.*. **6**, 155-161 (2000,9)

[13] Badrossamay, M. & Childs, T. Further studies in selective laser melting of stainless and tool steel powders. *Int. J. Mach. Tools Manuf.*. **47**, 779-784 (2007,4)

[14] Li, Y. & Gu, D. Thermal behavior during selective laser melting of commercially pure titanium powder: Numerical simulation and experimental study. *Addit. Manuf.*. **1-4** pp. 99-109 (2014,10)

[15] Criales, L., Arısoy, Y. & Özel, T. Sensitivity analysis of material and process parameters in finite element modeling of selective laser melting of Inconel 625. *Int. J. Adv. Manuf. Technol.*. **86**, 2653-2666 (2016,10)

[16] Fu, C. & Guo, Y. 3-Dimensional Finite Element Modeling of Selective Laser Melting Ti-6Al-4V Alloy. (2014,8)

[17] Yadroitsev, I. & Smurov, I. Selective laser melting technology: From the single laser melted track stability to 3D parts of complex shape. *Phys. Procedia*. **5** pp. 551-560 (2010)

[18] Rasch, M., Roider, C., Kohl, S., Strauß, J., Maurer, N., Nagulin, K. & Schmidt, M. Shaped laser beam profiles for heat conduction welding of aluminium-copper alloys. *Opt. Lasers Eng.*. **115** pp. 179-189 (2019,4)

[19] Grünewald, J., Gehringer, F., Schmöller, M. & Wudy, K. Influence of ring-shaped beam profiles on process stability and productivity in laser-based powder bed fusion of AISI 316L. *Metals (Basel)*. **11**, 1989 (2021,12)

[20] Mohammadpour, M., Wang, L., Kong, F. & Kovacevic, R. Adjustable ring mode and single beam fiber lasers: A performance comparison. *Manuf. Lett.*. **25** pp. 50-55 (2020,8)

[21] Wessels, H., Weißenfels, C. & Wriggers, P. Metal particle fusion analysis for additive manufacturing using the stabilized optimal transportation meshfree method. *Comput. Methods Appl. Mech. Eng.*. **339** pp. 91-114 (2018,9)

[22] Denlinger, E., Gouge, M., Irwin, J. & Michaleris, P. Thermomechanical model development and in situ experimental validation of the Laser Powder-Bed Fusion process. *Addit. Manuf.*. **16** pp. 73-80 (2017,8)

[23] Kamara, A., Wang, W., Marimuthu, S. & Li, L. Modelling of the melt pool geometry in the laser deposition of nickel alloys using the anisotropic enhanced thermal conductivity approach. *Proc. Inst. Mech. Eng. Pt. B: J. Eng. Manuf.*. **225**, 87-99 (2011,1)

[24] Becker, T., Stark, T., Arduini, M., Manara, J. & Altenburg, S. Knowing the spectral directional emissivity of 316L and AlSi10Mg PBF-LB/M surfaces: gamechanger for quantitative in situ monitoring. *Prog. Addit. Manuf.*. (2024,5)

[25] Huang, Z., Jia, W., Wang, H., Yang, Z., Li, C., Liang, J. & Zhong, Y. A new heat source model for selective laser melting simulations based on energy distribution on the powder layer and the surface of substrate. (arXiv,2021)

[26] Zhang, S., Fan, Z., Li, J., Wen, S., Paddea, S., Lu, L. & Li, S. Experimental characterisation and numerical modelling of residual stresses in a nuclear safe-end dissimilar metal weld joint. *Metals (Basel)*. **11**, 1298 (2021,8)

[27] Rossman, C.,private communication, (2024,05)

[28] Mills, K. Recommended Values of Thermophysical Properties for Selected Commercial Alloys. (Woodhead,2002)

A

Appendix 1

The script used to run the transient thermal simulations:

```
from additivemanufacturing.analysis import prepare_scanningpath_analysis
from fem.util import jobutil

addlab.initialize_new_database()
addlab.workdir = os.path.join(os.environ['HOMEPATH'], 'Desktop', 'Scanning')

if not os.path.exists(addlab.workdir):
    os.mkdir(addlab.workdir)

# here we define the model's dimensions

hobjid = addlab.create_scanningpath_simulation_mesh(objid='ScanningMesh',
    w=6, # model width
    h=1.2, # model height
    d=1, # model depth
    nw=120, # number of elements in width
    nh=30, # number of elements in height
    nd=12, # number of elements in depth
    laserline=True)


# here we load the material properties    #addlab.get_material_data_from_library(
matprop = {'Tmelt': 1.3990e+03, #[degC]
 'rho': 7.990e-09, # [ton/(mm^3)]
 'k': 1.3670e+01,  # [mW/(mm*K)]
 'c': 4.4700e+08,  # [mJ/(ton*K)]
 'E': 2.0457e+05,  # [N/(mm^2)]
 'nu': 2.8534e-01, # [-]
 'Re': 2.8392e+02, # [N/(mm^2)]
 'Rm': 6.1579e+02, # [N/(mm^2)]
 'em': 5.000e-01,  # [-]
 'alpha': 1.5916e-05, # [1/K]
 'exx': -4.7136e-03, # [-]
 'eyy': -4.7136e-03, # [-]
 'ezz': -1.6368e-04, # [-]
 'exy': 0.0, # [-]
```

```
 'eyz': 0.0, # [-]
 'exz': 0.0, # [-]
 'temperature_dependent': {
 'DENSITY':
[[7.9900e-09, 2.5000e+01],
 [7.9600e-09, 1.0000e+02],
 [7.9200e-09, 2.0000e+02],
 [7.8700e-09, 3.0000e+02],
 [7.8200e-09, 4.0000e+02],
 [7.7700e-09, 5.0000e+02],
 [7.7300e-09, 6.0000e+02],
 [7.6800e-09, 7.0000e+02],
 [7.6300e-09, 8.0000e+02],
 [7.5800e-09, 9.0000e+02],
 [7.5300e-09, 1.0000e+03],
 [7.4800e-09, 1.1000e+03],
 [7.4300e-09, 1.2000e+03],
 [7.3700e-09, 1.3000e+03],
 [7.3200e-09, 1.4000e+03],
 [6.0122e-09, 2.7540e+03]],

 'CONDUCTIVITY':
[[1.3670e+01, 2.5000e+01],
 [1.4670e+01, 1.0000e+02],
 [1.6000e+01, 2.0000e+02],
 [1.7340e+01, 3.0000e+02],
 [1.8680e+01, 4.0000e+02],
 [2.0010e+01, 5.0000e+02],
 [2.1350e+01, 6.0000e+02],
 [2.2690e+01, 7.0000e+02],
 [2.4020e+01, 8.0000e+02],
 [2.5360e+01, 9.0000e+02],
 [2.6690e+01, 1.0000e+03],
 [2.8030e+01, 1.1000e+03],
 [2.9360e+01, 1.2000e+03],
 [3.0700e+01, 1.3000e+03],
 [3.2280e+01, 1.4000e+03],
 [3.2793e+01, 1.4220e+03]],

 'SPECIFIC HEAT':
[[4.4700e+08, 2.5000e+01],
 [4.6800e+08, 1.0000e+02],
 [4.8900e+08, 2.0000e+02],
 [5.0700e+08, 3.0000e+02],
 [5.2400e+08, 4.0000e+02],
 [5.4000e+08, 5.0000e+02],
```

```
 [5.5700e+08, 6.0000e+02],
 [5.7400e+08, 7.0000e+02],
 [5.9200e+08, 8.0000e+02],
 [6.1000e+08, 9.0000e+02],
 [6.2800e+08, 1.0000e+03],
 [6.4800e+08, 1.1000e+03],
 [6.6800e+08, 1.2000e+03],
 [6.8800e+08, 1.3000e+03],
 [8.5200e+08, 1.4000e+03],
 [8.5817e+08, 1.5560e+03]],

 'ELASTIC':
[[2.0457e+05, 2.8434e-01, 2.0000e+01],
 [7.3735e+04, 2.5785e-01, 1.2090e+03]], #default additive lab

'EXPANSION, TYPE=ORTHO':
[[1.5916e-05, 1.5916e-05, 1.5916e-07, 20.0],
 [2.0171e-05, 2.0171e-05, 2.0171e-07, 1343.0]], #default additive Lab

 'PLASTIC':
[[2.8392e+02, 0.0000e+00, 2.0000e+01],
 [2.8392e+02, 0.1000e-01, 2.0000e+01],
 [9.9339e+01, 0.0000e+00, 8.7100e+02],
  [9.9339e+01, 0.1000e-01, 8.7100e+02]]},
 'Name': 'AM316L literature'}



# here we define the scanning path
scanningpath = [[
    110, # laser power [W]
    0.30, # radius of the laser spot [mm]
    0.52, # absorption coefficient [-]
    100, # scanning speed [mm/s]
    0.55, # X starting coordinate of the laser [mm]
    0.6, # Y starting coordinate of the laser [mm]
    1, # Z starting coordinate of the laser [mm]
    5.55, # X end coordinate of the laser [mm]
    0.6, # Y end coordinate of the laser [mm]
    1, # Z end coordinate of the laser [mm]
    "G", # laser shape profile either 'G' for gaussian or 'C' for cylindrical
    2.0,  # If a gaussian profile is used this is the gaussian shape factor
    0.12 #effective LPD, from estimated value of 0.17 Foroozmehr
]]

jobdir = os.path.join(addlab.workdir, 'Therm')
```

```
jobname = "ScanningPathSim"
runfname = prepare_scanningpath_analysis(hobjid,
    addlab.get_object_by_id(hobjid),
    jobname,
    os.path.join(addlab.workdir, 'Therm'),
    matprop,
    scanningpath,
    temp_init=20, temp_chamber=20, temp_bp=20, temp_cool_down=20,
    simtype="Therm",
    nout=['U', 'NT'], eout=['E', 'PEEQ', 'S', 'NOE'], solver='DEFAULT',
    t_cool_down=1,      #time of cooling after laser,
    phasechange=True,
    pwd_conv=0.001,       #[mW/mm^2k]convection of powder, need to motivate, shoul
    Pwdcondcorr=0.01,     #[-] from Foroozmehr
    Pwdstiffcorr=0.001,   #Needs motivation, value is from additive lab user manua
    tinit_heat=1e-4,          #time of first timestep.
    bp_conv=0.0,          #[mW/mm^2k]Assume no flux since powder is reletively thi
    top_conv=0.01,          #[mW/mm^2k] top convection, assumed natural convection
    top_emissivity=0.0,   #top radiation Needs motivation
    outputfrequ_heat=25,
    temperature_depentent=True)

jobutil.execute_fem_batchfile(os.getcwd(), jobdir, runfname)
resultfname = uf.rmbs(os.path.join(jobdir, jobname + '_SIM.addlabres'))
resobjid = addlab.get_new_result_id(hobjid, 'Therm')
modid = addlab.get_model_of_object(hobjid)
resobjid = addlab.import_addlabres(resultfname,
    modid=modid,
    mattribute="Results")
addlab.hide_object(hobjid)
addlab.on_set_orientation_to_iso()
addlab.update_tree()
```

B

Appendix 2

The script used to run the Thermo-mechanical simulation. Note: need to increase the maximum number of iterations

```
from additivemanufacturing.analysis import prepare_scanningpath_analysis
from fem.util import jobutil

addlab.initialize_new_database()
addlab.workdir = os.path.join(os.environ['HOMEPATH'], 'Desktop', 'Scanning')

if not os.path.exists(addlab.workdir):
    os.mkdir(addlab.workdir)

# here we define the model's dimensions

hobjid = addlab.create_scanningpath_simulation_mesh(objid='ScanningMesh',
    w=12, # model width (mm)
    h=1.2, # model height (mm)
    d=1, # model depth (mm)
    nw=120, # 100? number of elements in width
    nh=12, # 12? number of elements in height (even to have split in middle)
    nd=6, # 6? number of elements in depth
    laserline=True)


# here we load the material properties    #addlab.get_material_data_from_library(
matprop = {'Tmelt': 1.3990e+03, #[degC]
 'rho': 7.990e-09, # [ton/(mm^3)]
 'k': 1.3670e+01,  # [mW/(mm*K)]
 'c': 4.4700e+08,  # [mJ/(ton*K)]
 'E': 2.0457e+05,  # [N/(mm^2)]
 'nu': 2.8534e-01, # [-]
 'Re': 2.8392e+02, # [N/(mm^2)]
 'Rm': 6.1579e+02, # [N/(mm^2)]
 'em': 5.000e-01,  # [-]
 'alpha': 1.5916e-05, # [1/K] #value not used? I gave it temp dependant
 'exx': -4.7136e-03, # [-] need to get theese from Hussein? does it always use inh
 'eyy': -4.7136e-03, # [-]
 'ezz': -1.6368e-04, # [-]
```

```
 'exy': 0.0, # [-]
 'eyz': 0.0, # [-]
 'exz': 0.0, # [-]
 'temperature_dependent': {
 'DENSITY':
[[7.9900e-09, 2.5000e+01],
 [7.9600e-09, 1.0000e+02],
 [7.9200e-09, 2.0000e+02],
 [7.8700e-09, 3.0000e+02],
 [7.8200e-09, 4.0000e+02],
 [7.7700e-09, 5.0000e+02],
 [7.7300e-09, 6.0000e+02],
 [7.6800e-09, 7.0000e+02],
 [7.6300e-09, 8.0000e+02],
 [7.5800e-09, 9.0000e+02],
 [7.5300e-09, 1.0000e+03],
 [7.4800e-09, 1.1000e+03],
 [7.4300e-09, 1.2000e+03],
 [7.3700e-09, 1.3000e+03],
 [7.3200e-09, 1.4000e+03],
 [6.0122e-09, 2.7540e+03]],

 'CONDUCTIVITY':
[[1.3670e+01, 2.5000e+01],
 [1.4670e+01, 1.0000e+02],
 [1.6000e+01, 2.0000e+02],
 [1.7340e+01, 3.0000e+02],
 [1.8680e+01, 4.0000e+02],
 [2.0010e+01, 5.0000e+02],
 [2.1350e+01, 6.0000e+02],
 [2.2690e+01, 7.0000e+02],
 [2.4020e+01, 8.0000e+02],
 [2.5360e+01, 9.0000e+02],
 [2.6690e+01, 1.0000e+03],
 [2.8030e+01, 1.1000e+03],
 [2.9360e+01, 1.2000e+03],
 [3.0700e+01, 1.3000e+03],
 [3.2280e+01, 1.4000e+03],
 [3.2793e+01, 1.4220e+03]],

 'SPECIFIC HEAT': #(from MH)keep from foroozmehr, gives better comparison to earli
[[4.4700e+08, 2.5000e+01],
 [4.6800e+08, 1.0000e+02],
 [4.8900e+08, 2.0000e+02],
 [5.0700e+08, 3.0000e+02],
 [5.2400e+08, 4.0000e+02],
```

```
 [5.4000e+08, 5.0000e+02],
 [5.5700e+08, 6.0000e+02],
 [5.7400e+08, 7.0000e+02],
 [5.9200e+08, 8.0000e+02],
 [6.1000e+08, 9.0000e+02],
 [6.2800e+08, 1.0000e+03],
 [6.4800e+08, 1.1000e+03],
 [6.6800e+08, 1.2000e+03],
 [6.8800e+08, 1.3000e+03],
 [8.5200e+08, 1.4000e+03],
 [8.5817e+08, 1.5560e+03]],

 'ELASTIC': #From hussein E[N/(mm^2)] from GPa to MPa
[[198.5e+03, 0.3, 25],
[187e+03, 0.3, 200],
[172e+03, 0.3, 400],
[157e+03, 0.3, 600],
[141e+03, 0.3, 700],
[106e+03, 0.3, 800],
[10e+03, 0.3, 1300]],

'EXPANSION': #from Hussein [alpha, temp]
[[1.43e-05, 25],
[1.56e-05, 200],
[1.69e-05, 400],
[1.77e-05, 600],
[1.85e-05, 700],
[1.91e-05, 800],
[1.95e-05, 1300]],

 'PLASTIC': # [MPa, plastic strain, temp] have to give this for yelding? not reall
[[282, 0, 25],
[217, 0, 200],
[161, 0, 400],
[153, 0, 600],
[108, 0, 700],
[50, 0, 800],
[5, 0, 1300]]},
 'Name': 'AM316L literature'}



# here we define the scanning path
scanningpath = [[
    100, # laser power [W]
    0.075, # radius of the laser spot [mm]
```

```
    0.3, # absorption coefficient [-]
    100, # scanning speed [mm/s]
    1, # X starting coordinate of the laser [mm]
    0.6, # Y starting coordinate of the laser [mm]
    1, # Z starting coordinate of the laser [mm]
    11, # X end coordinate of the laser [mm]
    0.6, # Y end coordinate of the laser [mm]
    1, # Z end coordinate of the laser [mm]
    "G", # laser shape profile either 'G' for gaussian or 'C' for cylindrical
    2.0,  # If a gaussian profile is used this is the gaussian shape factor
]]

jobdir = os.path.join(addlab.workdir, 'ThermMech')
jobname = "ScanningPathSim"
runfname = prepare_scanningpath_analysis(hobjid,
    addlab.get_object_by_id(hobjid),
    jobname,
    os.path.join(addlab.workdir, 'ThermMech'),
    matprop,
    scanningpath,
    temp_init=26.85, temp_chamber=26.85, temp_bp=26.85, temp_cool_down=26.85, #Huss
    simtype="ThermMech",
    nout=['U', 'NT'], eout=['E', 'PEEQ', 'S', 'NOE'], solver='DEFAULT',
    t_cool_down=2,      #time of cooling after laser,
    phasechange=True,
    pwd_conv=0.001,       #[mW/mm^2k]generally low, here a tenth of the top convet
    Pwdcondcorr=0.01,     #[-] from Foroozmehr
    Pwdstiffcorr=0.001,   #Needs motivation, value is from additive lab user manua
    tinit_heat=1e-4,          #time of first timestep.
    bp_conv=0.0,          #[mW/mm^2k]Assume no flux since powder is reletively thi
    top_conv=0.02,          #[mW/mm^2k] top convection, assumed natural convection
    top_emissivity=0,     #No radiation in Hussein
    outputfrequ_heat=25,  #change back to 25
    cvgalpha=-0.33)

jobutil.execute_fem_batchfile(os.getcwd(), jobdir, runfname)
resultfname = uf.rmbs(os.path.join(jobdir, jobname + '_SIM.addlabres'))
resobjid = addlab.get_new_result_id(hobjid, 'ThermMech')
modid = addlab.get_model_of_object(hobjid)
resobjid = addlab.import_addlabres(resultfname,
    modid=modid,
    mattribute="Results")
addlab.hide_object(hobjid)
addlab.on_set_orientation_to_iso()
addlab.update_tree()
```

C

Appendix 3

The script used to retrive the data from

```
no_of_steps = len(addlab.get_all_step_names())
import numpy as np
from ux.dialogs import *
import model.object
ISOVALUE = 1399.0

for j in range(1,no_of_steps):
    Step = "STEP %i" % (int)(j)

    addlab.plot_result(stepname=Step, resultvar="STRESS")
    #"NDTEMP", "STRESS", "DISP"
    objid = addlab.get_active_object_id()
    obj = addlab.get_object_by_id(objid)
    resultvar = addlab.get_current_result_variable(objid)
    nids=[10199]
    coords, res = obj.get_node_results()

    #nids = obj.get_selected_node_ids(intids=True)
    #nids=[46854] #foroozmehr
    nids=[10199]  # Hussein
    coords, res = obj.get_node_results(getmagnitude=False)
    val = res[nids].flatten()

    klukka= obj.get_time_of_step(Step)
    print('Time of step: %1e' % (klukka))
    print(val)
```

D

Appendix 3

The script used to determine the melt-pool dimensions

```
from ux.dialogs import *

# enter an iso-value to draw a blue contour
ISOVALUE = None
if hasattr(addlab, 'ISOVALUE'):
    ISOVALUE = addlab.ISOVALUE

# grab data.
objid = addlab.get_active_object_id()
obj = addlab.get_object_by_id(objid)

resultvar = addlab.get_current_result_variable(objid)

    if ISOVALUE is None and resultvar == 'NDTEMP':
        try:
            # Obtaining the melting temperature from the utilized material data
            # in the resultobject
            val = obj.fem_data['Simparam']['matprop']['Tmelt']
            ISOVALUE = f'{val:1.1f}'
        except:
            ISOVALUE = '1390.0'

    ISOVALUE = TextEntry('Temperature', descriptor='Enter threshold value', value=I
    if ISOVALUE is not None:
        addlab.ISOVALUE = ISOVALUE

    if ISOVALUE is not None:

        ISOVALUE = float(ISOVALUE)

        # Obtaining the results and result coordinates
        coords, res = obj.get_node_results()
        connectivity = obj.get_connectivity(intids=True)

        int_eids = np.where(np.any(res[connectivity] >= ISOVALUE, axis=1))[0]
```

```
    # Uncomment the line below to see the elements that form the melt pool
    obj.select_elements(int_eids, intids=True)

    # determine melt pool dimensions
    dx = coords[[connectivity[int_eids]], 0].max() - coords[[connectivity[int_e
    dy = coords[[connectivity[int_eids]], 1].max() - coords[[connectivity[int_e
    dz = coords[[connectivity[int_eids]], 2].max() - coords[[connectivity[int_e

    v_mp = 0.0
    for eid in int_eids:
        conn = connectivity[eid]
        ecoords = coords[conn]
        a = (np.sum((ecoords[1] - ecoords[0]) ** 2)) ** 0.5
        b = (np.sum((ecoords[2] - ecoords[1]) ** 2)) ** 0.5
        c = (np.sum((ecoords[4] - ecoords[0]) ** 2)) ** 0.5
        v_elem = a * b * c

        # Here we are checking how many of the nodes are
        # actually reaching /exceeding the melting temperature
        # and scale the volume accordingly in a simplified approach.
        fact = np.sum(res[conn] >= ISOVALUE) / len(conn)

        v_mp += v_elem * fact

    print('Melt-pool dimensions: dx: %1.3e, dy: %1.3e, dz: %1.3e' % (dx, dy, dz
    print('Melt-pool volume: %1.5e' % (v_mp))
    return(v_mp)
```